

A characterization of clouds and precipitation over the Southern Ocean from synoptic to micro scales during the CAPRICORN field campaigns

Estefania Montoya Duque¹, Yi HUANG², Steven Siems³, Peter May⁴, Alain Protat⁵, and Greg McFarquhar⁶

¹University of Melbourne

²The University of Melbourne

³MONASH UNIVERSITY

⁴Monash University

⁵Australian Bureau of Meteorology

⁶Cooperative Institutes for Mesoscale Meteorological Studies

November 22, 2022

Abstract

The persistent Southern Ocean (SO) shortwave radiation biases in climate models and reanalyses have been associated with the poor representation of clouds, precipitation, aerosols, the atmospheric boundary layer, and their intrinsic interactions. Capitalizing on shipborne observations collected during the Clouds Aerosols Precipitation Radiation and atmospheric Composition Over the Southern Ocean (CAPRICORN) 2016 and 2018 field campaigns, this research investigates and characterizes cloud and precipitation processes from synoptic to micro scales. Distinct cloud and precipitation regimes are found to correspond to the seven thermodynamic clusters established using a K-means clustering technique, while less distinctions are evident using the cyclone and (cold) front compositing methods. Cloud radar and disdrometer data reveal that light precipitation is common over the SO with higher intensities associated with cyclonic and warm frontal regions. While multiple microphysical processes and properties are present in several cloud regimes, ice aggregation appears to be dominant in deep precipitating clouds. Mixed phase, and in some cases, riming was detected in shallow convective clouds away from the frontal conditions. Two unique clusters with contrasting cloud and precipitation properties are observed over the high-latitude SO and coastal Antarctica, suggesting distinct physical processes therein. Through a single case study, in-situ and remote-sensing data collected by an overflight of the Southern Ocean Clouds Radiation Aerosol Transport Experimental Study (SOCRATES) were also evaluated and complement the ship-based analysis.

1 **A characterization of clouds and precipitation over the**
2 **Southern Ocean from synoptic to micro scales during**
3 **the CAPRICORN field campaigns**

4 **E. Montoya Duque^{1,2}, Y. Huang^{1,2}, S.T. Siems^{2,3}, P.T. May³, A. Protat⁴, G.**
5 **M. McFarquhar^{5,6}**

6 ¹The University of Melbourne, Melbourne, Australia

7 ²Australian Research Council Centre of Excellence for Climate Extremes, Melbourne, Australia

8 ³Monash University, Melbourne, Australia

9 ⁴Australian Bureau of Meteorology, Melbourne, Australia

10 ⁵Cooperative Institute for Severe and High Impact Weather Research and Operations (CIWRO)

11 ⁶School of Meteorology, University of Oklahoma, Norman, OK, USA

12 **Key Points:**

- 13 • Distinct cloud and precipitation regimes correspond to the diverse Southern Ocean
14 synoptics, defined using a K-means clustering technique
15 • Evidence shows multiple microphysical features, like mixed phase in shallow con-
16 vection and ice aggregation in deep precipitating clouds
17 • Two unique clusters with contrasting cloud and precipitation properties are over
18 the high-latitude region, where models have large biases

Corresponding author: Estefania Montoya Duque, emontoyaduqu@student.unimelb.edu.au

Abstract

The persistent Southern Ocean (SO) shortwave radiation biases in climate models and reanalyses have been associated with the poor representation of clouds, precipitation, aerosols, the atmospheric boundary layer, and their intrinsic interactions. Capitalizing on shipborne observations collected during the Clouds Aerosols Precipitation Radiation and atmospheric Composition Over the Southern Ocean (CAPRICORN) 2016 and 2018 field campaigns, this research investigates and characterizes cloud and precipitation processes from synoptic to micro scales. Distinct cloud and precipitation regimes are found to correspond to the seven thermodynamic clusters established using a K-means clustering technique, while less distinctions are evident using the cyclone and (cold) front compositing methods. Cloud radar and disdrometer data reveal that light precipitation is common over the SO with higher intensities associated with cyclonic and warm frontal regions. While multiple microphysical processes and properties are present in several cloud regimes, ice aggregation appears to be dominant in deep precipitating clouds. Mixed phase, and in some cases, riming was detected in shallow convective clouds away from the frontal conditions. Two unique clusters with contrasting cloud and precipitation properties are observed over the high-latitude SO and coastal Antarctica, suggesting distinct physical processes therein. Through a single case study, in-situ and remote-sensing data collected by an overflight of the Southern Ocean Clouds Radiation Aerosol Transport Experimental Study (SOCRATES) were also evaluated and complement the ship-based analysis.

Plain Language Summary

The current generation of climate models and reanalyses products have difficulties in properly representing the radiative balance over the Southern Ocean (SO), which can be traced to the poor understanding of clouds and precipitation processes in this region. The remote location of the SO is a key factor for the lack of field observations that allow the scientific community to address the above-mentioned problem. However, recent coordinated field campaigns have collected an unprecedented amount of data, offering new opportunities to explore this understudied region. This research paper aims to study clouds and precipitation processes over the SO using shipborne data collected from two field campaigns in 2016 and 2018. Using different synoptic classification techniques, we identify unique macro and micro cloud and precipitation behaviors that correspond to the various weather patterns across a wide range of latitudes. In addition, we use aircraft observations collected from an overflight to evaluate and complement our analysis of the shipborne data. The study offers a framework that may help better understand the nature of the model biases over the SO.

1 Introduction

The Southern Ocean (SO) is a region of significant interest for its capacity to store excess heat and carbon. Yet large shortwave radiative biases over the SO continue to exist in both climate models and reanalysis products, which are primarily attributed to the poor representation of clouds, precipitation, aerosols, and their interactions in this region (Bodas-Salcedo et al., 2012, 2014; Kay et al., 2016; Zelinka et al., 2020; McFarquhar et al., 2021). These errors limit the ability of models to predict climate in this region, and the associated global climate feedbacks (Bodas-Salcedo et al., 2014; Ceppi et al., 2016; Gettelman et al., 2019).

While many studies have found that an incorrect ice-liquid partitioning, typically in the cold sector of extratropical cyclones (Bodas-Salcedo et al., 2012; Williams et al., 2013; Bodas-Salcedo et al., 2014; Naud et al., 2014), constitutes a leading cause of the model biases, mechanisms that are responsible for these deficiencies are not yet clear. In addition, compensating errors associated with multi-layer clouds (Protat et al., 2017), biases in the frontal region of extratropical cyclones (Kelleher & Grise, 2019), as well as

69 errors in shallow cyclones near the Antarctic continent (Mason et al., 2015) have all been
70 documented. These findings underline the complicated nature of the models biases and
71 the dynamical and physical processes at play.

72 The challenges in understanding and modeling the SO climate has helped motivate
73 a number of recent international field campaigns with the aim to improve the fundamen-
74 tal understanding of key atmospheric processes in this region through coordinated air-
75 craft, shipborne and ground-based observations. Among these efforts, four recent col-
76 laborative field campaigns funded by agencies in the United States and Australia are sum-
77 marized in McFarquhar et al. (2021). These projects include i) The Clouds Aerosols Pre-
78 cipitation Radiation and atmospheric Composition Over the Southern Ocean (CAPRI-
79 CORN), 2016 and 2018; ii) The Macquarie Island Cloud Radiation Experiment (MICRE),
80 2016-2018; iii) The Measurements of Aerosol, Radiation, and Clouds over the Southern
81 Ocean (MARCUS), 2017-2018; iv) The Southern Ocean Cloud Radiation and Aerosol
82 Transport Experimental Study (SOCRATES), 2018.

83 The comprehensive measurements collected from these projects are being utilized
84 to examine clouds, aerosols, precipitation and radiation characteristics over the SO in
85 unprecedented detail. Using remote-sensing and in-situ observations, recent studies have
86 refined our understanding of the bulk statistics of cloud occurrence and phase partition-
87 ing (Mace & Protat, 2018a), properties of non-precipitating liquid-phase low-level clouds
88 (e.g. Mace and Protat (2018b), Mace et al. (2021)), as well as cloud properties in the
89 cold sector of extratropical cyclones (e.g. Y. Wang et al. (2020), D’Alessandro et al. (2021),
90 Zaremba et al. (2020)). Case studies have also been carried out to examine special phe-
91 nomena such as an atmospheric river (Finlon et al., 2020), mesoscale cellular convection
92 (Lang et al., 2021), and convective generating cells near the cloud tops (Alexander et al.,
93 2021; Y. Wang et al., 2020). These new observations have also enabled the evaluation
94 of model simulations across a range of spatial and temporal scales (e.g. Protat et al. (2017),
95 Atlas et al. (2020), Zhou et al. (2020), Gettelman et al. (2020)).

96 Despite the significant advancements, many key questions remain unaddressed. One
97 under-studied area is the understanding of processes involved in the life cycle of precip-
98 itation. Previous studies using precipitation records from Macquarie Island have iden-
99 tified the prevalence of drizzle and light precipitation and linked their bulk statistics to
100 frontal and cyclonic activities (Z. Wang et al., 2015; Lang et al., 2018). More broadly,
101 however, precipitation properties across the SO are largely unknown. Model errors in
102 precipitation processes, such as the long-standing "warm-rain" process errors, remain
103 widespread in the latest generation of climate models, which bias cloud feedbacks by as
104 much as the CMIP5-to-CMIP6 climate sensitivity difference (Mülmenstädt et al., 2021).

105 Moreover, fewer studies have thus far focused on understanding the thermodynamic
106 structure of the lower troposphere and how it controls the cloud-precipitation proper-
107 ties and processes over the SO, within the context of synoptic meteorology. Understand-
108 ing these relationships is of importance, as the thermodynamics is arguably the largest
109 term in water budget between different cloud types (McCoy et al., 2021). It is benefi-
110 cial to explore these relationships at shorter timescales, given the transient nature of the
111 weather systems that dominate the mid- and high-latitudes (Kelleher & Grise, 2019).
112 Such practice is also a necessary step towards developing a physical, process-level un-
113 derstanding that is required for constraining the cloud-precipitation processes while mit-
114 igating compensating process errors in climate models (Mülmenstädt et al., 2021).

115 Using the collection of 2186 atmospheric soundings from the above-mentioned field
116 campaigns, a recent study by Truong et al. (2020) was among the first to examine the
117 relationships between the synoptic meteorology and lower tropospheric thermodynamic
118 structure over the SO, using a K-means clustering complemented by front and cyclone
119 composite analyses. The authors identified seven distinct clusters, which uniquely rep-
120 resent the various thermodynamic conditions over the SO, extending the knowledge de-

121 rived from a 16-year record of soundings from Macquarie Island, where the mid-latitude
 122 storm track clusters dominate (Lang et al., 2018).

123 Built upon the analysis in Truong et al. (2020), the aim of this study is to exam-
 124 ine cloud-precipitation properties and processes within the context of thermodynamic
 125 clusters as well as front and cyclone composites, using the shipborne observations col-
 126 lected from CAPRICORN experiments. In particular, we seek to address two questions:
 127 (1) Are there distinct cloud regimes that correspond to the unique thermodynamic and
 128 synoptic conditions? (2) How do the microphysics and precipitation processes differ in
 129 the various cloud regimes and atmospheric environments? We also present a case study,
 130 where we combine remote-sensing and in-situ observations from CAPRICORN and SOCRATES
 131 during a short overflight to provide further insights into the interplay between multiple
 132 processes. The description of the data and methods is presented in Section 2. Results
 133 are in Sections 3 and 4. Finally, the discussion and conclusions are in Section 5.

134 2 Data and Methods

135 2.1 Field Campaigns

136 The CAPRICORN field campaign was conducted with the RV Investigator, oper-
 137 ated by the Australian Marine National Facility, consisting of two voyages led by the Aus-
 138 tralian Bureau of Meteorology (BoM). The first voyage (CAPRICORN I) was carried
 139 out from 13 March to 15 April 2016, traversing in the Australian water between Hobart,
 140 Australia (42.8°S, 147.3°E) and around 55°S. CAPRICORN II was executed in austral
 141 summer (from 11 January to 21 February 2018) and had a broader latitudinal coverage
 142 (from Hobart to around 64°S). As the ship track was primarily designed to meet oceanog-
 143 raphic objectives, the RV Investigator sometimes remained at the same station for 6-
 144 24 hours, commonly at high latitudes poleward of the oceanic polar front. Together these
 145 two voyages produce a rich dataset encompassing clouds, aerosols, precipitation and ra-
 146 diation measurements over the Australian sector of the SO (McFarquhar et al., 2021).

147 The Southern Ocean Cloud Radiation and Aerosol Transport Experimental Study
 148 (SOCRATES) campaign undertook 15 research flights from Hobart to near 62°S (134-
 149 163°E) during January-February of 2018 (Y. Wang et al., 2020). The flights were un-
 150 dertaken with the NSF/NCAR HIAPER Gulfstream V (GV) aircraft, making in-situ and
 151 airborne remote-sensing measurements of cloud, aerosol, and planetary boundary layer
 152 (PBL) properties, including (but not limited to) the structures and vertical distributions
 153 of liquid and mixed-phase clouds and aerosols. The flights were designed to sample the
 154 cold sectors of extratropical cyclones, where many climate models have the largest ra-
 155 diation biases (Marchand et al., 2014; McFarquhar et al., 2021).

156 2.2 Remote sensing data

157 Both the RV Investigator and the GV HIAPER included Doppler cloud radar (see
 158 Table 1), allowing for an opportunity to obtain synchronous cloud radar data during over-
 159 flight periods. As has been established in the literature (e.g. Bodas-Salcedo et al. (2011),
 160 Huang et al. (2015)), a cloud radar detects different types of ice and water particles. For
 161 an in-cloud temperature less than 0°C, reflectivities larger than 5 dBZ commonly indi-
 162 cate a cloud dominated by large ice particles. 5 dBZ or less usually indicate Super-cooled
 163 Liquid Water (SLW) and/or small ice particles (including their coexistence). Instead,
 164 for temperatures greater than 0°C, liquid non-precipitating clouds are typically repre-
 165 sented by a reflectivity lower than -15 dBZ, drizzle by radar reflectivities between -15
 166 and -7.5 dBZ; precipitating clouds by a reflectivity larger than -7.5 dBZ. The cloud radar
 167 from the CAPRICORN field campaigns also measured Doppler velocity, which is a com-
 168 bination of falling particles' speed and vertical wind speed. Different ice habits have dis-
 169 tinct falling speeds, making it difficult to identify the type of ice. Nevertheless, we can

170
171

deduce the likely presence of certain ice forming mechanism by the reflectivity, Doppler velocity, and temperature range.

Table 1. Remote sensors and in-situ instruments deployed on the RV Investigator and GV (HIAPER) aircraft during the CAPRICORN and SOCRATES field campaigns.

Instrument Name	Description	Measurement Ranges	Key Variables
Remote sensors/CAPRICORN			
Cloud radar BASTA ^{1*} Delanoë et al. (2016), UCAR/NCAR EOL (2018)	W-band cloud radar 94.95 GHz. Mounted on a stabilized platform to endure vertical radar points.	Temporal resolution 12 s and four vertical resolutions (12.5, 25, 100, 200 m). Minimum valid signal distance 40 m, maximum observable altitude 12 km minimum detectable radar reflectivity -45 dBZ at 1 km. Time: 1 min	Reflectivity, Doppler velocity.
In-situ/CAPRICORN			
ODM470 Disdrometer Klepp et al. (2018)	OceanRAIN ^{2*} dataset. Emits a light from a diode at 880 nm and measure a volume of 120 nm in diameter. 1 minute resolution. 128 bins with logarithmic increase from 0.1 to 20 nm in diameter.	Very light (0.01-0.09 mm/hr), light (0.1-0.99 mm/hr), moderate (1-9.99 mm/hr), intense (10-49.99 mm/hr), extreme (above 50 mm/hr)	Precipitation rate, intensity, and phase.
Remote Sensors/SOCRATES			
Cloud radar HIAPER HCR ^{3*} Vivekanandan et al. (2015) UCAR/NCAR - EOL (2014) NCAR/EOL (2023)	W-band cloud radar 94.4 GHz.	Resolution 30-150 m, sensitivity of -39.6 dBZ at 1 km, radial velocity uncertainty 0.2 m s ⁻¹ at a vertical velocity of 2 m s ⁻¹ . Time: 0.5 s (corresponding to a spatial resolution of 83-105m.	Reflectivity, Doppler velocity
In-situ cloud probes/SOCRATES			
Two-Dimensional Cloud Probe (2DC) Wu and McFarquhar (2016)	Cloud optical array imaging probe with 64 photodiodes, a 25 μm resolution. Sample volume is a function of Diameter (D)	D: > 200 μm IWC: derived following Baker and Lawson (2006)	IWC, Nice, Dmm ^{4*} , cloud particle images
Cloud Droplet Probe (CDP) Lance et al. (2010)	Forward scattering probe that sizes particles using the Mie Theory. It emits a light from a laser beam and measures droplets (no ice)	Diameter: 2-50 μm	LWC, Nc
Particle Habit Imaging and Polar Scattering Probe (PHIPS HALO) Abdelmonem et al. (2016), Schnaiter et al. (2018), Järvinen et al. (2022, Under Review)	Two stereo microscopic cameras and detectors for measuring the scattering of light	Detecting particles from 20 to 700 μm of diameter (for ice, the lower diameter range is 50 μm)	Particle images, multi-angular scattering
Rosemount Icing Detector (RICE) Baumgardner and Rodi (1989)	Piezoelectric sensor which detects presence of SLW.	Minimum SLW detected is 2 mVm^{-1} McFarquhar et al. (2013)	Voltage change
State parameters/SOCRATES			
Vertical Cavity Surface Emitting Laser Hygrometer (VCSEL) Diao, M. (2018)	Lase based hygrometer.	Water Vapor concentrations	Relative Humidity

1* BASTA (Bistatic Radar System for Atmospheric Studies).

2* OceanRAIN (Ocean Rainfall And Ice-phase precipitation measurement Network).

3* HIAPER (High-Performance Instrumented Airborne Platform for Environmental Research).

4* Liquid Water Content (LWC), Ice Water Content (IWC), particle number concentration (Nc), Ice number concentration (Nice), median mass diameter (Dmm). Super-Cooled Liquid Water (SLW), particle size (D).

172

2.3 In-situ data

173

174

175

176

177

178

179

180

181

182

183

184

185

186

To measure surface precipitation, the RV Investigator employed an ODM470 disdrometer, which is part of the OceanRAIN dataset (Ocean Rainfall And Ice-phase precipitation measurement Network, Klepp et al. (2018)), see table 1. Values below 0.01 mm/hr and spurious data are set to zero (refer to Klepp et al. (2018) for details on the intensity labeling). Note that the thermodynamic phase has inherent uncertainties in the estimated precipitation rates for mixed and snow phase precipitation (Klepp et al., 2018). Our initial analysis has identified two precipitation events with a 1-minute precipitation rate apparently exceeding 100 mm/hr (2018-01-27 22:00 to 23:13 UTC, and 2018-02-09 around 10:50 UTC). While these events have been classified as extreme, the actual precipitation rates are subject to very large uncertainties and are likely affected by the presence of ice and so should be treated with caution. All values above 101 mm/hr (99.85% percentile which represent 0.021% of the total data) are excluded in the present analysis. The threshold is selected based on the inspection of the disdrometer time series and cross-examination of the C-band radar during those times.

187

188

189

190

191

192

193

194

195

196

197

198

199

200

201

202

203

204

A number of in-situ cloud microphysics datasets from the SOCRATES field campaign (Table 1) are also analyzed for a case study during one overflight transect above the RV Investigator (Section 3.4) (UCAR/NCAR EOL, 2019; Wu & McFarquhar, 2019; Schnaiter, 2018). Detailed information on the processing of in-situ cloud probe data and an overview of the uncertainties of the derived products and cloud parameters are provided in Y. Wang et al. (2020), McFarquhar et al. (2021), D’Alessandro et al. (2021), Baumgardner et al. (2017), and McFarquhar et al. (2017). It is worth highlighting that the 2DC is used in this analysis even though McFarquhar et al. (2021) stated that the use of the 2DS (which measures particles with similar sizes) was preferential because the 2DC suffered frequent fogging issues during SOCRATES. However, for the time period analyzed, the 2DS was suffering from technical issues. A careful inspection of the 2DC images for the analyzed period did not show any evidence of degraded image quality. For other time periods without degraded 2DC image quality and available 2DS data, Schima et al. (2022, In Preparation) showed that the 2DC had a slight underestimation of N_c by a factor varying between 0.5 and 0.75 (e.g., for flight on 4 February 2018). Corrections for out of focus particles, and shattered particles are made following techniques referenced above and incorporated into the University of Illinois/Oklahoma Optical Array Probe Processing Software (UIOOPS, McFarquhar et al. (2018)).

205

2.4 Synoptic and thermodynamic conditions

206

207

208

209

210

211

212

213

214

215

216

217

218

219

220

221

222

In this study, we characterize clouds and precipitation under various atmospheric conditions using three different, but complementary methods: clusters, cyclone composites and cold front composites. First, is the seven thermodynamic clusters defined in Truong et al. (2020) which are found to be able to represent the mid-latitude storm track region (M1-M4), cyclones over the high-latitude SO (C1) and the sub-Antarctic (coastal) waters (C2) (Figure 1). We also use traditional synoptic classifications for constructing composites: cyclone and frontal activity detection. Extratropical cyclones are detected with the University of Melbourne (UM) cyclone detecting and tracking scheme using the 3-hourly ERA5 reanalysis product at a 0.25° spatial resolution (Murray & Simmonds, 1991). The UM cyclone tracking and detecting method is a well-established global method for cyclone detection (Pepler et al., 2020). For a given cyclone, we define four quadrants as in Lang et al. (2018) (Q1-Q4; within a distance up to 15° from the cyclone center) and one center (Q0; representing all soundings within 5° distance of the cyclone center). Fronts are detected using the method of Berry et al. (2011) with hourly ERA5 reanalysis at a 0.75° spatial resolution. Only cold fronts within 15° from the RV Investigator are considered. The cold Frontal sections are defined as distances within 2.5° of the front line, whereas the pre-frontal (post-frontal) sections are between -15 and -2.5° (2.5 and 15°).

223
224

A schematic diagram that describes the general relationships between the various classifications are presented in Figure 1.

225
226
227
228
229
230

It is worth noting that the weather conditions over the SO are highly variable. Thus, the location of warm and cold fronts relative to the cyclone center can differ significantly from the classic diagram shown in Figure 1. Also, the spatial and temporal resolution of ERA5 used for the cyclone and front detection can induce uncertainties in their exact positions. Nevertheless, the seven clusters extend beyond the common storm-track weather patterns typically represented in the cyclone and front composites.

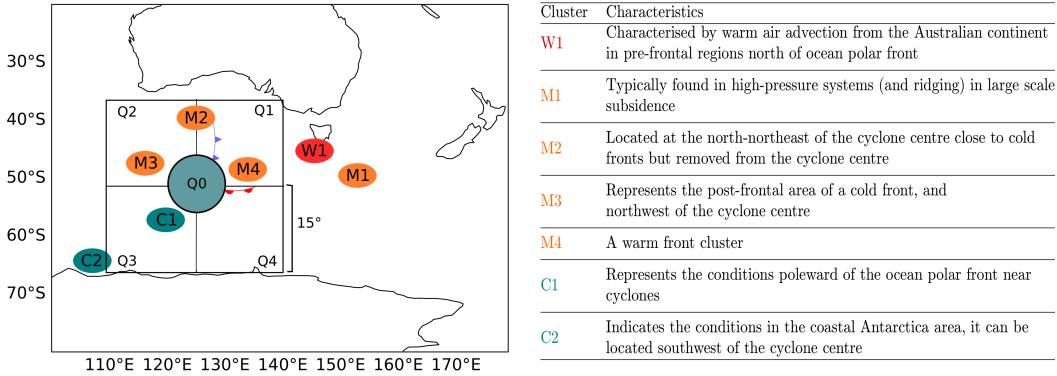


Figure 1. A conceptual illustration of the seven thermodynamic clusters and their relationships to the extratropical cyclone, cold and warm front, derived in Truong et al. (2020). The red circle indicates the warm cluster (W1), Orange circles the medium clusters (M1-M4), and dark blue circles the cold clusters (C1-C2) and the proximity to Q0. Q0 represents the cyclone center, Q1-Q4 indicate the four cyclone quadrants. The red (blue) curve with half-circles (triangles) indicates the warm (cold) front. Note that cold and warm fronts are not always within the above illustrated quadrants. On the right, main cluster characteristics are also presented.

231
232
233
234
235
236
237
238

Of the 2186 soundings employed in Truong et al. (2020), 266 were from CAPRI-CORN 2016 and 2018. To analyze the clouds and precipitation associated with each of these sounding profiles and the corresponding cluster, cyclone and front, data are taken within ± 1.5 hours of each sounding’s launch time (see Table 2 for the number of sounding per classification). The length of the time window was chosen to ensure that the ship traveled less than 1 degree, yet provided enough samples for a robust statistical analysis. Time windows from ± 0.5 to 4.0 hours were tested, but did not qualitatively change the results.

239

3 Cloud and precipitation properties

240
241
242
243
244
245
246
247
248
249

To provide insights into the thermodynamic phase and microphysical processes of the observed clouds and precipitation, Contoured Frequency by Altitude Diagram (CFAD, Yuter and Houze (1995)) and a variant, Contour Frequency by Temperature Diagram (CFTD, Huang et al. (2015)) are constructed from the RV Investigator cloud radar reflectivity for the various synoptic classifications. These diagrams do not assume prior statistics, so they can be used for non-Gaussian and multi-modal distributions such as radar data since they preserve the information in the frequency distribution (Yuter & Houze, 1995). Additionally, we consider the median radar reflectivity as a function of the Doppler velocity and temperature (altitude) (Figures 2, 3 and 4). We note that the CFTD is able to clearly define the melting level, which may be of particular interest. The cloud mask

product from the CAPRICORN cloud radar and lidar information (Huang et al., 2019) is used to estimate cloud cover percentage, which is defined as the ratio between the time when cloud was observed over the ship and the total length of the time-window for a given synoptic condition.

The received power by the cloud radar is affected by the particle size observed such that the radar is sensitive to large particles. As such the composite structures of the radar reflectivity and Doppler velocity can be examined jointly to infer plausible dominant ice growth processes, when the known limitations of a single-frequency cloud radar are properly taken into account. For instance, given the low density and large size of ice aggregates compared to liquid drops, aggregation is likely dominant when the reflectivity in the temperature range (-30 to -15°C) increases more uniformly towards lower altitudes (higher temperatures), while the Doppler velocity remains relatively small (between 0 and -1 ms^{-1} , Thompson et al. (2008)) yet exhibiting a similar tendency. On the other hand, strong riming may be present when moderate-to-strong reflectivities are accompanied by higher fall velocities, particularly at the sub-freezing temperature range in a convective environment where supersaturation with respect to liquid water is more easily achieved.

We consider both surface and in-cloud precipitation. The shipborne disdrometer records are used to determine the 1-minute surface precipitation rates and the thermodynamic phase (see section 2.3). In-cloud precipitation is defined as precipitation that is developed in clouds but does not reach the surface at the ship. In-cloud precipitation is considered when the minimum radar reflectivity profile above 0.2 km exceeds -15 dBZ (lower threshold for drizzle), and the disdrometer detects dry conditions at the surface. We note that in-cloud precipitation has the potential to advect far downwind in the strong westerly winds of the SO storm track. Thus in-cloud precipitation does not necessarily indicate sub-cloud evaporation.

3.1 Cloud radar statistics under the seven K-Means clusters

The CFTD/CFAD of the W1 cluster (warm air advection in the pre-frontal regions north of ocean polar front) is characterized by a broad distribution of clouds across the temperature range from -30 to 15°C, reaching altitudes up to almost 8 km (Figure 2a, c). The large fraction of warm clouds (greater than 0°C) features a wide reflectivity spectrum between -25 and 10 dBZ, indicating a large variability ranging from non-precipitating to drizzling, to precipitating clouds. Precipitating warm clouds typically have Doppler velocity less than -3 ms^{-1} with median reflectivities higher than 5 dBZ, indicating some heavy falls. Drizzling and non-precipitating warm clouds correspond to a weaker Doppler velocity; between 0 and -1 ms^{-1} (Figure 2b, d). The average melting layer height is identified at around 3 km, the highest of all clusters (Figure 2c, d). Between -10 and 0°C, precipitation-size particles dominate the reflectivities, with values between -10 and 5 dBZ (likely mixed-phase clouds), whereas clouds at temperatures less than -10°C have a core of strong reflectivities from -10 to 0 dBZ. The increase of reflectivity towards higher temperatures (between -15 and about -0°C) suggests ice particle growth likely via aggregation. Evidence of large ice particles (above 5 dBZ) associated with convective updrafts can be identified with Doppler velocities around 1 ms^{-1} at -20°C. Far less frequent, non-precipitating ice clouds (most likely cirrus) are also present, as shown in the second branch with temperatures below -10°C and reflectivities lower than -15 dBZ. Surface precipitation is recorded approx. 6% of the time, predominantly very light/light precipitation (below 0.99 mm/hr) and liquid phase (Table 2). Overall, these cloud and precipitation characteristics are consistent with warm air advection featuring a warm and moist troposphere.

The high-pressure cluster M1 (Figures 2e-h) features the lowest cloud cover percentage (CC 62%). A discontinuous dipole-like structure is evident in the CFTD/CFADs,

301 representing two dominant disconnected cloud types: non-/lightly precipitating bound-
 302 ary layer clouds (likely closed mesoscale cellular convection as reported in Lang et al.
 303 (2020), Lang et al. (2022)) with Doppler velocities between 0 to -2 ms^{-1} ; and mid-level
 304 clouds with in-cloud precipitation that does not reach the lower troposphere. The lat-
 305 ter features a high concentration around -20°C and -5 dBZ , which suggests small precipitation-
 306 size particles, possibly mixed phase. Cirrus clouds are also present (below -30°C and with
 307 reflectivities below -10 dBZ). Precipitation measurements suggest virtually dry condi-
 308 tions at the surface, and in-cloud precipitation about 7% of the time (Table 2). The dis-
 309 drometer measurements and the CFAD/CFTD cloud patterns are generally consistent
 310 with the M1 conditions inferred from the average sounding profile (Figure 3 in Truong
 311 et al. (2020)).

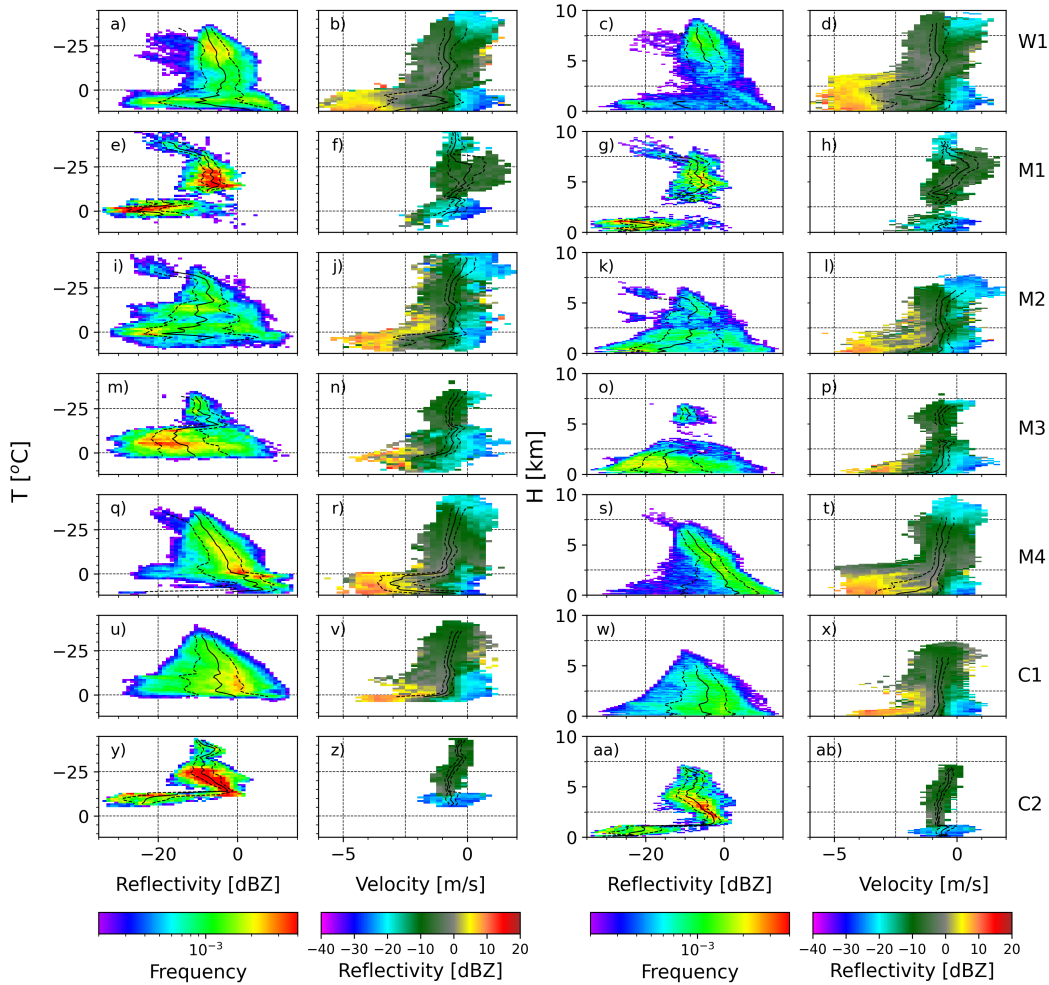


Figure 2. From left to right BASTA cloud radar reflectivity Contour Frequency by Temperature Diagram (CFAD) and reflectivity median value as a function of temperature and Doppler velocity, followed by the same figures for altitude. Dotted lines are the 25% and 75% percentile, line the 50% percentile of the abscissa variable. From top to bottom, clusters W1 (warm air advection), M1 (high pressure), M2 (cold front), M3 (post-front), M4 (warm front), C1 (high-latitude cyclone center), and C2 (coastal Antarctica). All during the CAPRICORN I and II, synoptic conditions are classified by a k-means clustering method.

312 Moving to the cold front (M2) cluster, the radar reflectivity CFTD/CFAD has a
 313 broad distribution (-25 to 15 dBZ), spanning from temperatures above 10°C down to about
 314 -15°C, hinting at a wide range of hydrometeor types/sizes, cloud types, microphysical
 315 processes, and convective/stratiform precipitation (Figures 2i, k). Strong radar reflectivities
 316 (greater than 5 dBZ) associated with Doppler velocity around/above 1 ms^{-1} are
 317 present between -20 and -5°C, consistent with strong ice production within the convective
 318 updraft. There are also some fast-falling particles, faster than -3 m/s, with reflectivities
 319 around 5 dBZ (Figure 2j, l). Between -30°C and -15°C, the slope of the mean
 320 reflectivity suggests ice growth. At around -35°C, the low reflectivities and narrow frequency
 321 distribution are consistent with ice deposition. Although one might expect considerable
 322 precipitation for the cold front cluster, the disdrometer indicates surface precipitation only 5%
 323 of the time: predominantly light (55%) and liquid (89%), followed by mixed phase (18%).
 324 The in-cloud precipitation is also only present $\sim 7\%$ of the time. While
 325 somewhat counter-intuitive, the analysis suggests that the M2 cluster might be dominated
 326 by pre-frontal multi-level clouds that do not actively produce intense precipitation.
 327

Table 2. 1 minute resolution OceanRAIN disdrometer surface precipitating time (P_s [%]), precipitating median \pm Interquartile range intensity ($\tilde{I} \pm IQR$ [mm/hr]), and percentages of surface very light (P_{vl}), light (P_l), moderate (P_m), intense (P_i), and extreme (P_e), as well as the percentage of liquid, snow and mixed-phase precipitation. Precipitating time inside clouds, and not reaching the surface (P_c [%]) estimated from the 1 minute mean W-band cloud radar. Cloud clover (CC) defined using the cloud mask from the cloud radar/lidar dataset on a 1-min resolution. All during CAPRICORN I and II classified by different synoptic scenarios: k-means clustering, distance to cyclone and front. Note that the number of soundings (S) used for the identification of each scenario is highlighted.

Synoptic	S	Disdrometer								Radar-lidar			
		P_s [%]	$\tilde{I} \pm IQR$ [mm/hr]	P_{vl} [%]	P_l [%]	P_m [%]	P_i [%]	P_e [%]	Liquid [%]	Snow [%]	Mixed [%]	P_c [%]	CC [%]
W1	39	6.30	0.27 \pm 0.9	31.06	44.71	23.29	0.94	0.00	100.00	0.00	0.00	13.08	83.80
M1	26	1.33	0.05 \pm 0.04	95.08	4.92	0.00	0.00	0.00	100.00	0.00	0.00	6.53	61.89
M2	41	4.54	0.24 \pm 0.55	28.35	55.49	15.85	0.30	0.00	89.02	0.61	10.37	6.69	71.86
M3	37	4.75	0.1 \pm 0.34	49.21	36.19	11.75	2.86	0.00	92.06	1.27	6.67	9.50	88.38
M4	21	44.92	0.37 \pm 0.78	28.10	51.36	20.48	0.00	0.06	96.81	1.77	1.42	10.60	92.19
C1	91	20.05	0.15 \pm 0.52	40.17	44.22	13.19	1.50	0.91	47.13	40.39	12.47	7.19	86.95
C2	11	0.00	0.00 \pm 0.00	0.00	0.00	0.00	0.00	0.00	0.00	0.00	0.00	21.57	85.41
Q0	57	23.15	0.21 \pm 0.52	32.38	53.12	14.24	0.22	0.04	67.98	21.76	10.26	8.50	92.22
Q1	40	14.79	0.28 \pm 0.77	35.17	45.54	19.09	0.10	0.10	90.21	4.84	4.94	10.25	70.70
Q2	39	10.57	0.17 \pm 0.88	40.91	35.81	20.66	2.62	0.00	94.49	2.75	2.75	7.78	84.45
Q3	36	6.72	0.09 \pm 0.1	55.89	39.26	4.62	0.23	0.00	25.87	73.67	0.46	8.14	76.91
Q4	29	18.26	0.55 \pm 1.04	15.55	53.89	23.84	3.78	2.94	78.00	5.57	17.44	12.03	87.50
Pre	45	10.27	0.19 \pm 0.42	30.59	63.46	5.94	0.00	0.00	71.30	28.70	0.00	8.37	82.30
Post	87	15.69	0.20 \pm 0.66	34.47	46.62	17.95	0.88	0.08	72.55	16.60	10.84	7.57	78.02
Frontal	26	23.13	0.40 \pm 0.93	32.44	43.19	23.35	1.02	0.00	73.21	17.05	9.73	3.93	95.38

328 The radar reflectivity CFTD/CFAD for the cold post-frontal (M3) cluster has a
 329 broad distribution in the lower troposphere, which narrows significantly towards higher
 330 (lower) altitudes (temperatures), signaling the dominance of a relatively shallow cloud
 331 population at temperatures greater than -15°C and a detached cloud between -35 and
 332 -15°C (Figure 2m, o). While non-precipitating clouds prevail in the shallow cloud regime,
 333 there are strong radar reflectivities (greater than 5 dBZ) associated with strong negative
 334 Doppler velocities (smaller than -2 ms^{-1}) between -10 and 0°C, consistent with the
 335 formation of large particles (Figure 2n, p). Such characteristics are congruent with in-situ
 336 observations in the Hallett-Mossop temperature zone shown in several previous studies
 337 for a similar synoptic environment (e.g. Huang et al. (2017), Huang et al. (2021)),

338 commonly associated with the open mesoscale cellular convection (Lang et al., 2021, 2022).
 339 Positive Doppler velocities indicate updrafts (convection) are stronger than for the M1
 340 cluster. Surface precipitation of this cluster is recorded 5% of the time, featuring dom-
 341 inantly very light/light precipitation and dominantly liquid phase. The bulk of the clouds
 342 residing below 2.5 km is consistent with a strong temperature inversion at approx. 780
 343 hPa for the M3 cluster (Figure 3 in Truong et al. (2020)).

344 The M4 cluster (warm front) produces the largest cloud cover (92%). The radar
 345 reflectivity CFTD/CFAD showcases the typical arc shape of large-scale deep convection,
 346 where the mean reflectivity increases monotonically towards higher temperatures and
 347 lower altitudes, which also indicates the likely presence of aggregation (Figure 2q, s). There
 348 is a visible enhancement of reflectivity below the melting level in the CFTD, but not ev-
 349 ident in the CFAD. This pattern suggests that the melting level in the M4 soundings varies
 350 across a range of altitudes. The frequency distribution in M4 is narrower than that in
 351 the M2 (cold front) cluster, indicating more uniform microphysical processes (likely dom-
 352 inated by aggregation, mainly between -15 and 0°C) as well as hydrometeor types. Strong
 353 reflectivity values in the warm rain region indicate precipitation with negative veloci-
 354 ties between -3 and -5 m s^{-1} (Figure 2q-t). This cluster registers the highest precipita-
 355 tion percentage (approx. 45% at the surface and 11% in clouds). The disdrometer records
 356 predominantly liquid phase (both warm rain and SLW). Overall the disdrometer and CFAD/CFTD
 357 information is consistent with a typical warm front scenario as discussed in Truong et
 358 al. (2020). The M4 and W1 clusters share some similarities in the CFAD/CFTD pat-
 359 terns, based on the nature of these two clusters we hypothesize that the W1 clouds evolve
 360 into M4 clouds as it moves further south. Additional analyses would be needed to con-
 361 firm this process.

362 The radar reflectivity CFTD/CFAD for the C1 cluster (high-latitude cyclone over
 363 the SO) feature an absence of warm clouds but a broad spectrum below freezing tem-
 364 perature, which indicates a wide variety of hydrometeors (Figure 2u-x). Unlike previ-
 365 ous clusters, there is no clear division between the cloud layers. Similar to M3, some of
 366 the high reflectivities coincide with fast falling velocities (smaller than -2 m s^{-1}) within
 367 the Hallett-Mossop temperature zone, possibly indicating the presence of rimed parti-
 368 cles and/or graupel, although further observations are needed to confirm the presence
 369 of this mechanism. High reflectivities associated with a Doppler velocity of around 1 m s^{-1}
 370 were also detected close to -15°C , suggestive of active convection. This is consistent with
 371 the expected behavior of C1, which resides typically close to a cyclone center. Precip-
 372 itation data show that C1 has the highest mean intensity from all clusters, although the
 373 absolute values are subject to higher uncertainties given the highest fraction of snow de-
 374 tected at the surface (about 40%).

375 Contrasting to the C1 cluster, the coastal Antarctica C2 cluster CFTD/CFAD in-
 376 dicates two distinct cold cloud types (Figure 2y, aa). One is the non-precipitating shal-
 377 low clouds (below 1 km or greater than -15°C) with radar reflectivities below -15 dBZ
 378 and Doppler velocities between -2 and 0.5 m s^{-1} (Figure 2z, ab). The other represents
 379 the mid-level cloud type which is more prevalent. The magnitude and slope of the re-
 380 flectivity frequencies between -30 to -15°C once again imply ice growth. The C2 clus-
 381 ter has no precipitation at the surface, consistent with the low humidity in the lower tro-
 382 posphere reported in Truong et al. (2020). However, in-cloud precipitation (not reach-
 383 ing the surface) is present almost 22% of the time in the mid-level clouds (Table 2), which
 384 suggests strong evaporation and/or sublimation in the lower troposphere, likely associ-
 385 ated with the descending, dry, katabatic winds off the Antarctic coast. Note that the num-
 386 ber of soundings for this cluster is relatively small (11) compared to the others.

387 It should be noted that the cluster classification performed by Truong et al. (2020)
 388 focused on the lower free troposphere, only employing soundings information up to the
 389 700 hPa level. In general, the upper troposphere has stronger winds and is not neces-
 390 sarily directly linked to the lower troposphere. We note the common presences of clouds

391 from 5 to 8km along the storm track (M1-M4). The strong winds in the upper-troposphere
 392 can readily advect clouds across the clusters. We also note that the cloud radar might
 393 under-detect the thin, non-precipitating liquid clouds, particularly in the lower tropo-
 394 sphere, but this limitation is not expected to affect our key findings.

395 **3.2 Cloud radar statistics under Cyclone Quadrants conditions**

396 Moving to the analysis with respect to cyclone quadrants, overall the CFAD/CFTD
 397 patterns corresponding to each quadrant are less distinct than those segregated by clus-
 398 ters (Section 3.1). Nevertheless, the zero quadrant (Q0) reflectivity CFTD/CFAD char-
 399 acteristics largely resemble the C1 counterparts, except that a small fraction of warm
 400 clouds are also present. This may be explained by the fact that Q0 includes all cyclone
 401 centers detected during the field campaigns, not only those limited to the high-latitude
 402 SO where clouds are generally much colder. Q0 also includes a portion of M2 (18%) and
 403 M4 (11%) clusters where warm clouds are not uncommon. The disdrometer information
 404 is consistent with the CFTD/CFAD analysis for Q0 in terms of precipitation character-
 405 istics.

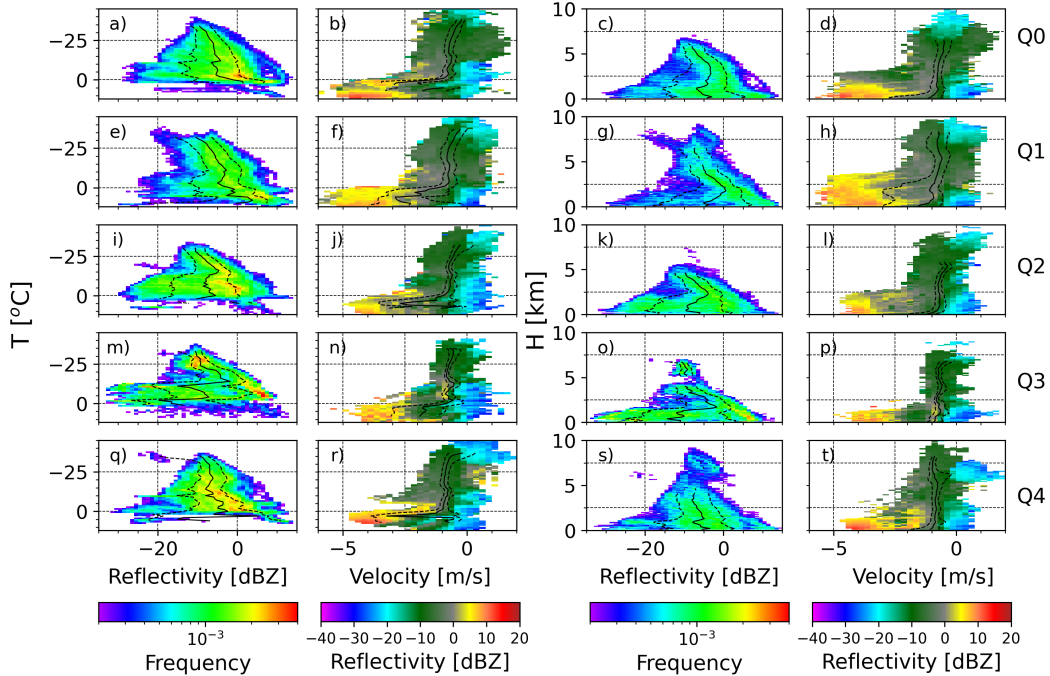


Figure 3. Same as Figure 2 but segregated by cyclone sectors.

406 Q1 resembles the M4 and M2 clusters, with differences noted due to the large vari-
 407 ability of the cold/warm front location with respect to the cyclone center. Thus, the Q1
 408 quadrant represents only a subset of the total number of cold and warm frontal condi-
 409 tions, whereas the M2 and M4 clusters showcase a more unambiguous representation.
 410 The Q1 CFTD/CFAD radar reflectivity has an arc shape between 5 and -10 dBZ (typ-
 411 ical of deep convection; Figures 3e-h). Warm clouds are mainly precipitating clouds with
 412 strong Doppler velocities between -6 and -2 ms^{-1} . Between -5 and 0°C there is a band
 413 ranging from 0 to -15 dBZ, suggesting mixed-phase conditions.

414 Q2 is likely dominated by shallow clouds at temperatures greater than -15°C (3
 415 km). The CFAD/CFTD distributions for Q2 are similar to those of the M3 cluster, which

416 is expected since the M3 cluster represents the post-frontal conditions. Several high-frequency
 417 cores are present between -15 and 0°C , indicating the presence of a variety of microphys-
 418 ical mechanisms (Figure 3i-l). Strong radar reflectivities (around 5 dBZ) are seen with
 419 Doppler velocities greater than -2 ms^{-1} , indicating the presence of dense particles (e.g.
 420 possibly graupel or rimed particles, as also noted for M3), as well as a mixture of liq-
 421 uid and ice precipitation. The surface precipitation characteristics also resemble those
 422 of M3.

423 Q3 and Q4 conditions are less explored in the literature. Our analysis suggests that
 424 Q3 is a hybrid of C1 and M3 conditions (Figure 3m, o) while Q4 most commonly rep-
 425 resents C1 and, to a lesser extent, W1 (Figure 3q-t.). Interestingly, however, Q3 has the
 426 lowest precipitation intensity among all cyclone sectors, while Q4 features the highest
 427 intensity. Q3 surface precipitation is dominated by snow, while liquid phase precipita-
 428 tion is most commonly observed for Q4 (mostly SLW). This may not be a surprise given
 429 the colder nature of Q3 associated with a stronger southerly winds.

430 It is worth noting that the 15° box per quadrant may not be the best threshold for
 431 discriminating the cyclone conditions, as the nearest cyclone may not necessarily be the
 432 dominant feature at a given sounding. Nevertheless, we tested three different sizes (from
 433 10 to 20° per quadrant) and the 15° was the distance that allowed a good number of sound-
 434 ing per quadrant. Our results are not qualitatively impacted by this threshold.

435 **3.3 Cloud radar statistics under cold Front distance conditions**

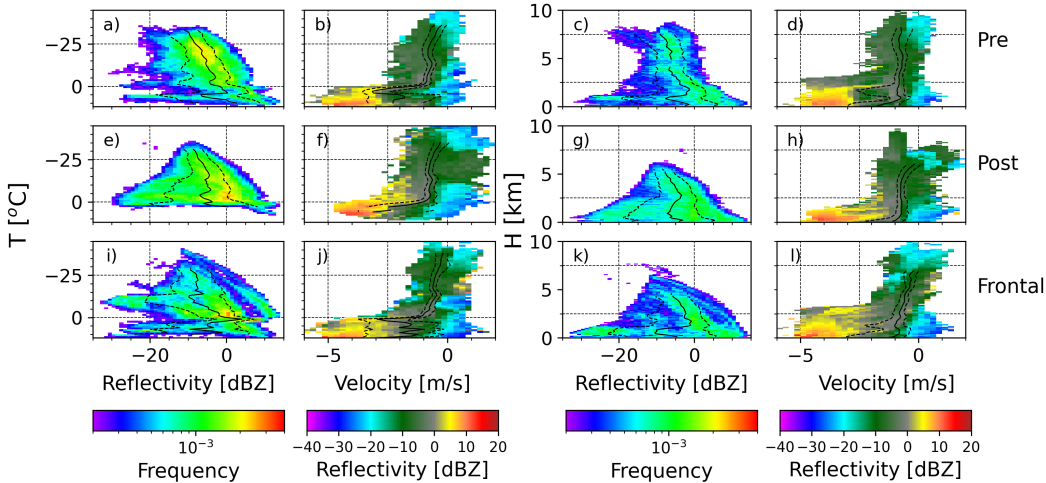


Figure 4. Same as Figure 2 but segregated by distance to cold front.

436 The analysis associated with cold front composites has significantly fewer sound-
 437 ings compared to the k-means clustering analysis (108 less). The pre-, post- and frontal
 438 classifications all have a hybrid of different clusters, suggesting that this methodology
 439 has limited skills in segregating cloud regimes.

440 The radar reflectivity CFTD/CFAD in the pre-frontal condition resemble that of
 441 the W1 cluster (Figure 4). It should be noted, however, that the W1 cluster only rep-
 442 resents the pre-frontal air mass with strong warm advection north of the ocean polar front,
 443 while the pre-frontal conditions could happen across latitudes. The post-frontal CFTD/CFAD
 444 distributions contain mainly some of the C1, M2, and M3. Finally, the cold frontal
 445 condition is composed primarily of almost the same proportion of C1 and W1 clusters.

446 Turning to precipitation, the pre-frontal condition has a higher fraction of warm
 447 rain, evidenced by the high reflectivity values at Doppler velocities stronger than -3 ms^{-1} .
 448 This classification also has the highest fraction of snow, according to the surface mea-
 449 surements. The frontal conditions have the highest precipitation intensity among the three,
 450 which is to be expected given the dominance of C1 (31%) and W1 (27%) clusters.

451 To summarize, the K-means clustering methodology is shown to be the most skill-
 452 ful in sorting/defining cloud and precipitation regimes. The cyclone and frontal compos-
 453 ite methods produced more ambiguous results, despite their extensive applications in the
 454 literature. In general, clouds in the upper free troposphere are less distinct across all clas-
 455 sifications, which is not unexpected given the common decoupling of the upper tropo-
 456 sphere dynamics from the surface meteorology that is used to drive the thermodynam-
 457 ics and synoptic classifications.

458 4 Case study: GV aircraft microphysical characteristics

459 In this section, we analyze a segment of the third flight (RF03) of the SOCRATES
 460 mission to evaluate, as a case study, our interpretation of remote-sensing observations
 461 from the CAPRICORN campaign. We selected the period when the GV aircraft was clos-
 462 est to the RV Investigator (between 2018-01-23 00:50 and 01:18 UTC), which is defined
 463 by the time the GV aircraft did one ascending (descending) leg towards (away from) the
 464 RV Investigator, sampling the same synoptic conditions (Figure 5). Since the shipborne
 465 cloud radar has a lower temporal resolution than the airborne one, we selected an ex-
 466 tended period for the comparison while ensuring that the ship was under the same syn-
 467 optic conditions (between 2018-01-22 23:40 and 2018-01-23 02:50 UTC).

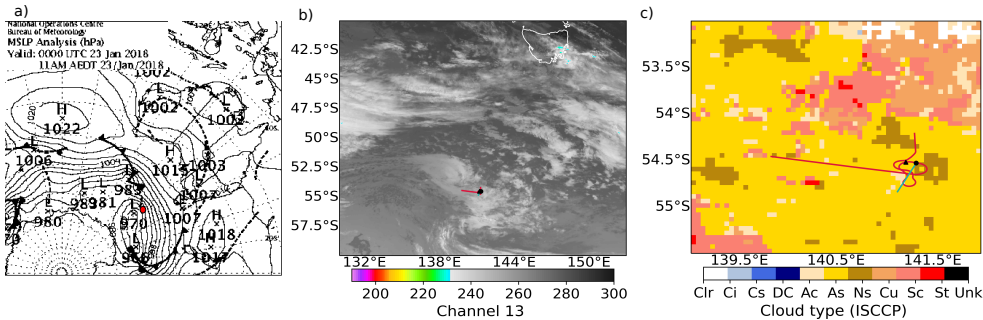


Figure 5. a) Mean Sea level Pressure (MSLP) analysis of the Australian Bureau of Meteorology (BoM) for 2018-01-23 00 UTC. Red dot indicates the approximate location of the RV investigator and the GV aircraft. b) Himawari-8 brightness temperature in Kelvin (channel 13), and c) cloud type classification from the Japan Aerospace Exploration Agency for 2018-01-23 00:50 UTC; black triangle (square) shows the location of the dropsonde (radiosonde). The red line indicates the GV aircraft track during the period (2018-01-23 00:50 to 01:18 UTC). Blue line represents the RV Investigator location while measuring the same type(s) of clouds (2018-01-22 23:40 and 2018-01-23 02:50 UTC).

468 Flight RF03 included one constant leg in the vicinity of the ship lasting for about
 469 7 minutes at 6 km, launching a dropsonde west of the RV Investigator at 2018-01-23 01:02
 470 UTC. The flight dropsonde is classified as a M4 cluster. Equally, the radiosonde from
 471 the RV Investigator, which was launched about 10 minutes before the approach of the
 472 aircraft (2018-01-23 00:52 UTC), is also classified as M4 (Figure 6). This is also consis-
 473 tent with the frontal and cyclone detection and the Himawari-8 satellite cloud type clas-

474 sification, with Altostratus, Nimbostratus and occasionally multi-layer cloud systems dom-
 475 inating the sampling area (Figure 5). The Mean Sea Level Pressure (MSLP) analysis chart
 476 from the BoM indicates the ship and the aircraft were located near a warm front at 2018-
 477 01-23 00:00 UTC, although at this time a low pressure center to the south was in close
 478 proximity. Note that the MSLP snapshot is earlier than the sampling period and the warm
 479 front would have been closer to the RV Investigator by the sampling time.

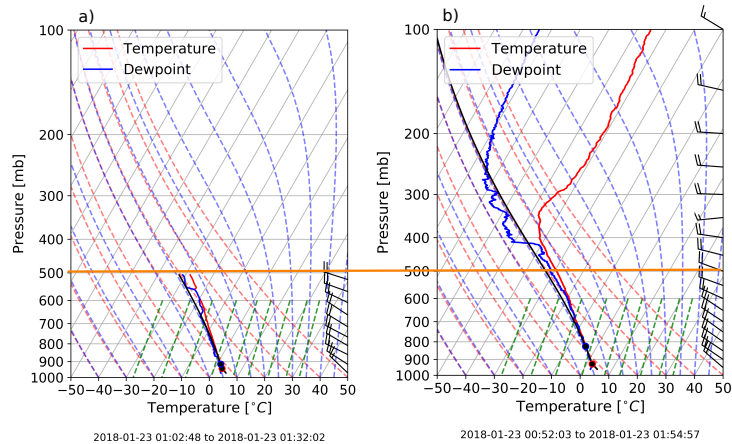


Figure 6. a) Dropsonde sounding profile from the GV aircraft launched at 2018-01-23 01:02 UTC. b) Radiosonde sounding released from the RV Investigator at 2018-01-23 00:52 UTC. Orange line indicates the altitude of the GV aircraft.

480 When using the other two synoptic classifications (cyclone and frontal composites),
 481 the sampled areas were in Q0 (at an approximate distance of 4° north 0.04° west of the
 482 cyclone center) and pre-frontal (at a distance of about 4° ahead of the cold front) con-
 483 ditions. When the ship and the aircraft were close, the radiosonde, the dropsonde, the
 484 radar and lidar observations show characteristics comparable to the M4 cluster descrip-
 485 tion. Both sondes indicate strong north-westerly winds and saturated conditions below
 486 500 hPa, indicating the presence of precipitating clouds (Figure 6). The disdrometer aboard
 487 the RV Investigator recorded primarily liquid precipitation with an intensity between very
 488 light to light and a median precipitation intensity of 0.14 ± 0.31 mm/hr. This is weaker
 489 than the median intensity in the M4 cluster, but still within the natural variability (0.21
 490 ± 0.52 mm/hr, Table 2).

491 The HIAPER radar observations show that the sampled clouds were commonly pre-
 492 cipitating (drizzle starts at -15 dBZ), with a melting layer located at around 600m above
 493 sea level (Figure 7). The Doppler velocity, ranging from 0.28 and -1.38 $m s^{-1}$, is predom-
 494 inantly negative and decreases further when reaching the melting layer (down to values
 495 near -5 $m s^{-1}$; Figure 7b). The radar reflectivity CFAD/CFTD features a broad distri-
 496 bution, suggesting a large variety of hydrometeors and microphysical types/processes (Fig-
 497 ure 8). Three modes of high frequency are visible: the first mode lies between -30 to $-$
 498 $10^\circ C$ (2.5 to 5 km), characterized by reflectivity increasing from -25 to 0 dBZ towards
 499 higher temperatures, likely suggesting particle growth primarily via aggregation. The
 500 second mode is located at -10 and $-5^\circ C$ (0.7 to 2 km), with reflectivities around -12
 501 and 0 dBZ, also suggesting ice growth. The third mode is a small core near the melting
 502 layer, likely indicating the coexistence of SLW and small ice particles. In the warm clouds,
 503 the radar reflectivities peak in the range of -15 to 0 dBZ, indicating lightly precipitating
 504 clouds. Although less frequent, the cloud radar also detects strong precipitation in the warm
 505 cloud region, where reflectivities above 5 dBZ, with Doppler velocities stronger than -3 $m s^{-1}$,

506 are present near the melting layer (Figures 8 a and c). The shipborne CFAD/CFTD pat-
 507 terns share some similarities with the GV counterparts, although the modes are less dis-
 508 tinct in the former probably due to the lower time resolution of the observations. Both
 509 the airborne and shipborne CFAD/CFTD patterns provide evidence of deep cloud layer(s)
 510 and particle growth towards lower altitudes via multiple mechanisms, broadly consistent
 511 with the M4 cluster and pre-frontal composite results as discussed in Section 3.

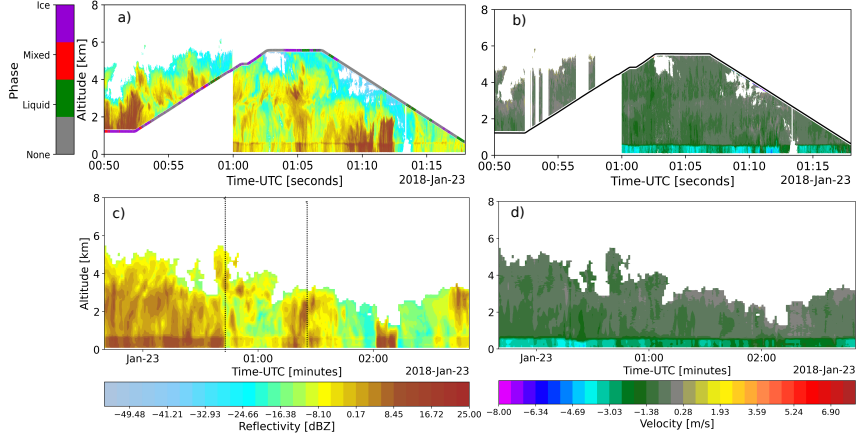


Figure 7. Upper panel shows the HIAPER (Aircraft) data from a) the cloud radar reflectivity (dBZ) (Contours), colored line indicates the GV altitude and phase classification according to Schima et al. (2022, In Preparation); and b) Doppler velocity between 2018-01-23 00:50 to 01:18 UTC. Lower panel indicates the ship based measurements of the BASTA c) cloud radar reflectivity (dBZ; dashed lines are the HIAPER time period), and d) Doppler velocity between 2018-01-22 23:40 and 2018-01-23 02:50 UTC. Note that the RV Investigator need more time to sample a similar area than the GV aircraft.

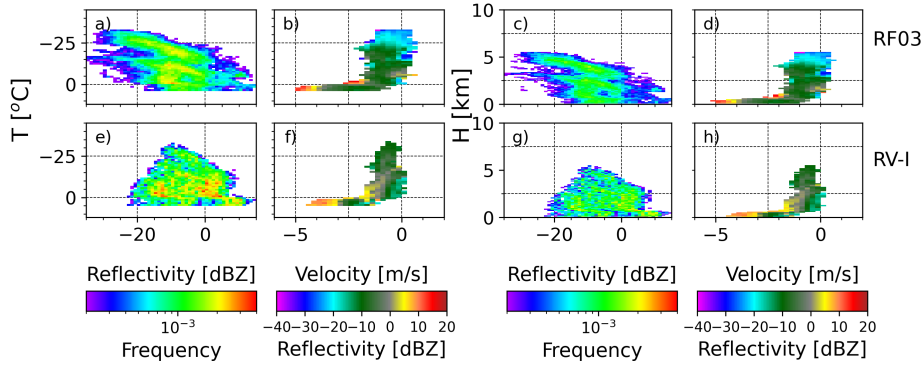


Figure 8. Same as Figure 2 but for the HIAPER cloud radar during the third flight of the SOCRATES field campaign (RF03) and the BASTA cloud radar during the CAPRICORN field campaign (RV-I). Note the time periods are different (2018-01-23 00:50 to 01:18 UTC vs 2018-01-22 23:40 and 2018-01-23 02:50 UTC; but both are under the same synoptic conditions (and cloud type)).

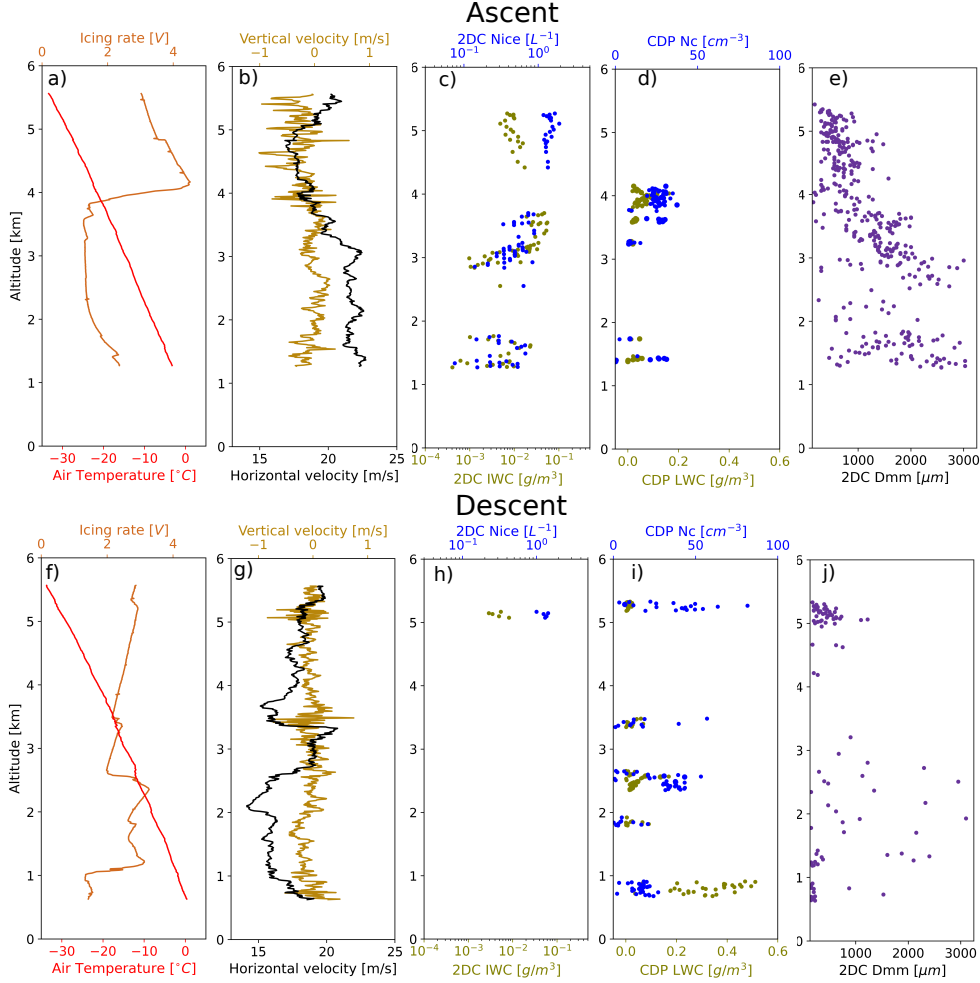


Figure 9. a,f) Temperature (red) and Supercooled Liquid Water (SLW, brown) proxy. b, g) Vertical (yellow) and horizontal (black) wind speed. c, h) 2DC Ice number concentration (Nice, blue) and Ice Water Content (IWC, green) derived for ice phase clouds only, d, i) CDP droplet concentration (Nc, blue) and Liquid Water Content (LWC, green) for mixed and liquid phase clouds. e, j) 2DC Median mass diameter (Dmm). For one ascending, descending leg during the GV aircraft overflight from the RV Investigator. Only values where the Total Water Content is $> 0.005 \text{ g/m}^{-3}$ are plotted.

512 The in-situ aircraft observations provide direct evidence of the microphysical properties that can help evaluate our interpretation from Figure 8. Here we examine one ascending and one descending leg in the proximity of the RV Investigator. The ascending leg penetrated through a deep cloud near a warm front, whereas the descending leg seemed to be coming through multi-layer clouds at the cloud edge and was not sampling much in cloud (Figure 7). The in-situ phase classification based on Schima et al. (2022, In Preparation) indicates that ice phase was dominant along the ascent profile, about 76% of the in-cloud time, largely coinciding with the enhanced radar reflectivities recorded in the vicinity of the flight path. The descent profile, on the other hand, features an intermittent presence of liquid or ice phase, consistent with the weaker reflectivities and the more tenuous structure of the cloud layers. The two vertical profiles show that the 2DC median mass diameter (Dmm) varies in the range between 150 and 3200 μm , suggesting

513
514
515
516
517
518
519
520
521
522
523

524 the common presence of large particles, particularly along the ascent profile (Figure 9).
 525 Consistently, the 2DC instrument detected ice number concentrations (Nice) through-
 526 out the ascent profile (especially around 1.5 km, 3 to 3.7 km, and near 5.3 km) in the
 527 range of 7.5×10^{-5} to $1.9 \times 10^{-3} \text{ cm}^{-3}$, whereas little Nice was recorded during the de-
 528 scending leg (Figures 9c and i, note that the Nice is shown for ice phase clouds only due
 529 to the large uncertainties in the estimated Nice for mixed phase using the 2DC). It should
 530 be noted that the Schima et al. (2022, In Preparation) phase classification indicates more
 531 frequent ice phase in the descent profile than Figure 9h, because the classification used
 532 a combination of several cloud probes, not only the 2DC where only particles sizes greater
 533 than $200 \mu\text{m}$ are considered. Liquid water content (LWC) profiles measured by the CDP
 534 probe are shown for liquid and mixed phase clouds (Figures 9d and i), providing more
 535 evidence on the phase characteristics. The descending leg further showcased typical bound-
 536 ary layer clouds (below 1 km; given the lower reached altitude).

537 The PHIPS particle habit images (Figure 10) indicate the frequent presence of rosettes
 538 at about 6 km or between -30 and -25°C . Some of the rosettes were bullet rosettes, while
 539 others have more complex structures. Between -20 and -10°C , the ice crystals were columns
 540 with some plate-like structures, rimed crystals, and ice of irregular habits (Figure 10).
 541 Between -5 and 0°C rimed particles and needles become more dominant, while water and
 542 rain droplets were typical at temperatures above 0°C . Snapshots of the particle images
 543 recorded by the Fast 2DC particle probe at different altitudes/temperatures also indi-
 544 cate a large variety of particle habits, broadly consistent with those recorded by the PHIPS
 545 instrument. Overall, the observed ice habits are consistent with what has been reported
 546 in the literature for deep clouds over mid and high latitude oceans (Bailey & Hallet, 2009;
 547 Kikuchi et al., 2013). Inspection of the 2DC images did not show evidence for pervasive
 548 amounts of supercooled drizzle (SLD). However, for small time periods there is a possi-
 549 bility that small amounts of SLD was present due to ambiguity in interpreting the shapes
 550 of the 2DC images, and hence in the phase.

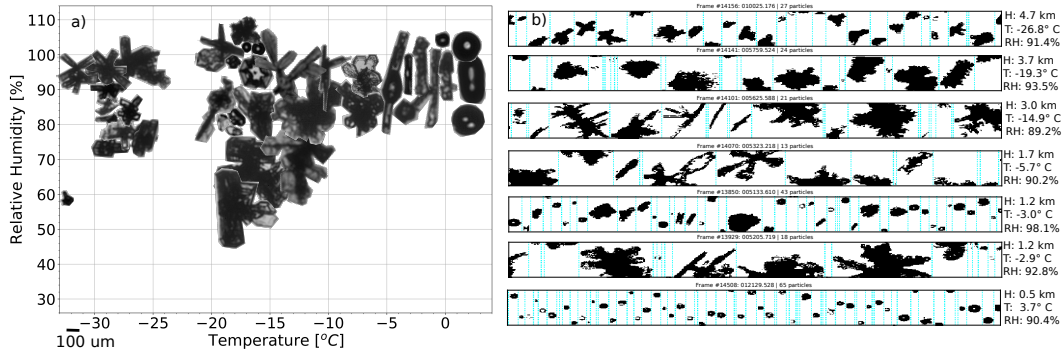


Figure 10. Particle images obtained by a) the Particle Habit Imaging and Polar Scattering (PHIPS-HALO) stereo imaging instrument. Images are represented as a function of temperature and relative humidity. b) The Fast 2DC probe. Both during the third flight of SOCRATES (RF03) in the vicinity of the RV Investigator (between 2018-01-23 00:20 to 01:29 UTC).

551 Overall, despite the somewhat non-classic warm front that was encountered dur-
 552 ing the overflight, the coincident airborne and shipborne radar reflectivity CFAD/CFTD
 553 analyses are largely consistent with the composite results in Section 3 for the M4 clus-
 554 ter. The limited in-situ cloud properties also support our interpretations of the CFAD/CFTD
 555 analysis and associated microphysical processes, although more data is necessary to en-
 556 hance the evaluation for other clusters.

5 Conclusions and Discussion

Motivated by the need to better understand the Southern Ocean (SO) cloud and precipitation systems, this research capitalized on recent field observations from the Clouds Aerosols Precipitation Radiation and atmospheric Composition Over the Southern Ocean (CAPRICORN) I and II to examine the macro- and microphysical characteristics of the clouds and precipitation, under different thermodynamic and synoptic atmospheric conditions. Aircraft observations collected by research flight RF03 from the Southern Ocean Clouds Radiation Aerosol Transport Experimental Study (SOCRATES) were used to complement the analysis and to evaluate the interpretations of the shipborne remote-sensing information. Key findings of this study include:

- Distinct cloud and precipitation regimes are found to correspond to the seven thermodynamic clusters established in Truong et al. (2020), over the Australian sector of the Southern Ocean. In contrast, cloud and precipitation regimes are less well defined using the cyclone and (cold) front compositing methods.
- The warm front (M4) and the high-latitude cyclone (C1) clusters possess the highest fractions of surface precipitation, with the former being dominated by warm rain and the latter featuring the largest fraction of snow. Evidence suggests that ice aggregation in relatively deep convection likely dominates the particle growth in M4, while multiple microphysical mechanisms within cold clouds are present in C1.
- The driest surface conditions are found to be associated with the Coastal Antarctica (C2) and high pressure (M1) clusters. Both represent a discontinuous dipole-like structure in the cloud vertical profiles, where low-level clouds are primarily non-precipitating.
- The warm air advection cluster (W1) is characterized by a variety of cloud processes featuring a warm, deep and moist troposphere. Unlike M4, only warm rain with a relatively weak intensity is recorded at the surface.
- The cold frontal (M2) and post-frontal (M3) clusters feature similar surface precipitation characteristics. However, the M2 cluster represents a higher variability of ice processes and cloud types, while M3 has a high frequency of mixed phase clouds between -15 and 0 °C.
- The case study using in-situ observations from SOCRATES generally supports the interpretations of key microphysical processes using the cloud radar profiles. A variety of ice habits are observed across a wide range of temperatures down to -35 °C under the M4 cluster.

The M3 cluster, which represents the cold sector of the cyclones over the mid-latitude SO, is characterized by the predominance of shallow clouds (below 3km and higher than -15 °C) that are composed primarily of non- to weakly precipitating particles in the lower troposphere. These clouds have been reported to be most poorly simulated in weather and climate model at all scales, constituting a leading contributor to the shortwave radiative biases (Bodas-Salcedo et al., 2012, 2014, 2016). However, it is worth noting that recent research has documented the frequent presence of both the open and closed Mesoscale Cellular Convective (MCC) clouds in this environment (Lang et al., 2021, 2022), with contrasting cloud phase composition and precipitation rates (Ahn et al., 2017; Huang et al., 2017, 2021). Further analysis into the oceanic and atmospheric conditions would be necessary to refine our understanding of the associated cloud controlling factors. However, we hypothesize that common presence of non- to weakly precipitating closed MCC clouds should influence by permitting less incoming radiation to the surface.

The cloud and precipitation characteristics associated with the high-latitude cyclones (C1) are intriguing, as the geographical distribution of this cluster is spatially more correlated with the locations of the largest radiative biases in climate model simulations

608 (Bodas-Salcedo et al., 2012). With the absence of warm clouds, ice (i.e. cold cloud) pro-
609 cesses are expected to be dominant in this environment. Our analysis presents evidence
610 of glaciation processes in these clouds, which are further supported by the largest frac-
611 tion of snowfall recorded at the surface. This creates an open question as how to rec-
612 oncile the prevailing argument on the lack of supercooled liquid water in climate mod-
613 els and the active glaciation evident in the ship observations over the high-latitude SO.
614 Equally interesting is the Coastal Antarctica (C2) cluster which is strongly dominated
615 by non-precipitating low clouds that are presumably mostly SLW, despite the precip-
616 itating clouds aloft. This is in sharp contrast to C1, and may be associated with the dry-
617 ing effect of the katabatic winds as discussed in Truong et al. (2020). Given that C2 clus-
618 ter had much fewer soundings from the CAPRICORN experiments, additional data would
619 be beneficial for a better characterization of this environment.

620 This study is the first, to our knowledge, to couple cloud and precipitation fields
621 with the thermodynamic and synoptic conditions over the remote SO using newly avail-
622 able field observations. Our analysis shows that, to a large extent, clouds and the en-
623 suant precipitation can be patterned by these atmospheric conditions. Leading micro-
624 physical processes are also inferred from the cloud radar reflectivities, Doppler velocity
625 and temperature ranges; however, these interpretations should only be treated as a first-
626 order, qualitative estimates that are in line with the given synoptic and thermodynam-
627 ical conditions. Different ice habits are characterized by distinct falling speeds, which
628 are difficult to distinguish using a single-frequency cloud radar. More in-situ data, to-
629 gether with innovative combinations of multiple remote-sensing observations, are needed
630 to validate these interpretations. Future studies should also consider evaluating the re-
631alism of the identified relationships in model simulations, with the aid of instrument sim-
632ulators.

633 Finally, while the cold-air sector of an extratropical cyclone possesses a large climatological-
634 mean bias, the day-to-day processes governing how the clouds respond to dynamical per-
635 turbations are more flawed in the anticyclones and the frontal environments, as elabo-
636 rated in a recent study where output from 10 models that participated in CMIP5 were
637 analyzed (Kelleher & Grise, 2019). Here our clustering framework would allow for a more
638 direct identification of processes that may be inherently misrepresented in models.

639 **Acknowledgments**

640 This work is supported by the Australian Research Council discovery grant DP190101362.
641 Y. Huang was also supported by the ARC Centre of Excellence for Climate Extremes
642 (CE170100023). G.M. McFarquhar was supported by the National Science Foundation
643 (NSF) through grants AGS-1628674 and AGS-1762096. The authors acknowledge the
644 thorough work from the CAPRICORN and SOCRATES teams to collect, post-processing,
645 and make available the datasets. The CAPRICORN data was collected using the RV In-
646 vestigator, we thank the CSIRO Marine National Facility (MNF), the ship’s personnel
647 and the scientific team for the efforts made in gathering and post-processing the infor-
648 mation. The data are publicly available from CSIRO Data Access Portal (<https://data.csiro.au/dap/>). The SOCRATES data were collected using NSF’s Lower Atmosphere
649 Observing Facilities, which are managed and operated by NCAR’s Earth Observing Lab-
650 oratory. The authors thank the pilots, mechanics, technicians, scientists, software en-
651 gineers, and project managers of the NCAR EOL Research Aviation Facility for their
652 support in the field and in post-processing data. The authors would like to thank the
653 Australian Bureau of Meteorology Tasmanian regional Office for the forecast support and
654 weather briefings provided during the field campaign with special thanks to Scott Car-
655 pentier, Michelle Hollister, Matthew Thomas, and Robert Schaap. The SOCRATES in-
656 formation can be found at the Earth Observing Laboratory (<http://catalog.eol.ucar.edu/socrates>). We sincerely thank Son Truong for providing the cluster classification
657
658

659 from CAPRICORN I and II field campaigns, Yang Wang and Julian Schima for giving
660 access to processed data used in the construction of Figure 9.

661 References

- 662 Abdelmonem, A., Järvinen, E., Duft, D., Hirst, E., Vogt, S., Leisner, T., &
663 Schnaiter, M. (2016). Phips-halo: the airborne particle habit imaging and
664 polar scattering probe – part 1: Design and operation. *Atmospheric Measure-*
665 *ment Techniques*, 9. doi: 10.5194/amt-9-3131-2016
- 666 Ahn, E., Huang, Y., Chubb, T. H., & Baumgardner, D. (2017). In situ observations
667 of wintertime low-altitude clouds over the Southern Ocean. *Quarterly Journal*
668 *of the Royal Meteorological Society*, 143. doi: 10.1002/qj.3011
- 669 Alexander, S. P., McFarquhar, G. M., Marchand, R., Protat, A., Vignon, E., Mace,
670 G. G., & Klekociuk, A. R. (2021). Mixed-phase clouds and precipitation in
671 southern ocean cyclones and cloud systems observed poleward of 64°s by ship-
672 based cloud radar and lidar. *Journal of Geophysical Research: Atmospheres*,
673 126. doi: <https://doi.org/10.1029/2020JD033626>
- 674 Atlas, R. L., Bretherton, C. S., Blossey, P. N., Gettelman, A., Bardeen, C., Lin,
675 P., & Ming, Y. (2020). How well do large-eddy simulations and global cli-
676 mate models represent observed boundary layer structures and low clouds over
677 the summertime Southern Ocean? *Journal of Advances in Modeling Earth*
678 *Systems*, 12. doi: <https://doi.org/10.1029/2020MS002205>
- 679 Bailey, M. P., & Hallet, J. (2009). A Comprehensive Habit Diagram for Atmospheric
680 Ice Crystals: Confirmation from the Laboratory, AIRS II, and Other Field
681 Studies. *Journal Atmospheric Sciences*, 66. doi: [https://doi.org/10.1175/](https://doi.org/10.1175/2009JAS2883.1)
682 [2009JAS2883.1](https://doi.org/10.1175/2009JAS2883.1)
- 683 Baker, B., & Lawson, R. P. (2006). Improvement in determination of ice water
684 content from two-dimensional particle imagery. part i: Image-to-mass relation-
685 ships. *Journal of Applied Meteorology and Climatology*, 45. Retrieved from
686 <http://www.jstor.org/stable/26171783>
- 687 Baumgardner, D., Abel, S. J., Axisa, D., Cotton, R., Crosier, J., Field, P., ... Um,
688 J. (2017). Cloud ice properties: In situ measurement challenges. *Meteorological*
689 *Monographs*, 58, 9.1-9.23. doi: 10.1175/AMSMONOGRAPHS-D-16-0011.1
- 690 Baumgardner, D., & Rodi, A. (1989). Laboratory and wind tunnel evaluations of the
691 rosemount icing detector. *Journal of Atmospheric and Oceanic Technology*, 6.
692 doi: [https://doi.org/10.1175/1520-0426\(1989\)006<0971:LAWTEO>2.0.CO;2](https://doi.org/10.1175/1520-0426(1989)006<0971:LAWTEO>2.0.CO;2)
- 693 Berry, G., Reeder, M. J., & Jakob, C. (2011). A global climatology of atmospheric
694 fronts. *Geophysical Research Letters*, 38. doi: [https://doi.org/10.1029/](https://doi.org/10.1029/2010GL046451)
695 [2010GL046451](https://doi.org/10.1029/2010GL046451)
- 696 Bodas-Salcedo, A., Andrews, T., Karmalkar, A. V., & Ringer, M. A. (2016). Cloud
697 liquid water path and radiative feedbacks over the southern ocean. *Geophysical*
698 *Research Letters*, 43. doi: <https://doi.org/10.1002/2016GL070770>
- 699 Bodas-Salcedo, A., Webb, M. J., Bony, S., Chepfer, H., Dufresne, J.-l., Klein,
700 S. A., ... John, V. O. (2011). COSP: Satellite simulation software for
701 model assessment. *Bulletin of the American Meteorological Society*, 92. doi:
702 [10.1175/2011BAMS2856.1](https://doi.org/10.1175/2011BAMS2856.1)
- 703 Bodas-Salcedo, A., Williams, K. D., & Field, P. R. (2012). The surface down-
704 welling solar radiation surplus over the southern ocean in the met office
705 model: The role of midlatitude cyclone clouds. *Journal of Climate*, 25. doi:
706 [10.1175/JCLI-D-11-00702.1](https://doi.org/10.1175/JCLI-D-11-00702.1)
- 707 Bodas-Salcedo, A., Williams, K. D., Ringer, M. A., Beau, I., Cole, J. N. S.,
708 Dufresne, J. L., ... Yokohata, T. (2014). Origins of the Solar Radiation
709 Biases over the Southern Ocean in CFMIP2 Models. *Journal of Climate*, 27.
710 doi: 10.1175/JCLI-D-13-00169.1
- 711 Ceppi, P., Zelinka, M. D., & Hartmann, D. L. (2016). The response of the south-

- ern hemispheric eddy-driven jet to future changes in shortwave radiation in
 cmip5. *Geophysical Research Letters*, 41. doi: <https://doi.org/10.1002/2014GL060043>
- D'Alessandro, J. J., McFarquhar, G. M., Wu, W., Stith, J. L., Jensen, J. B., &
 Rauber, R. M. (2021). Characterizing the occurrence and spatial heterogeneity
 of liquid, ice, and mixed phase low-level clouds over the southern ocean using
 in situ observations acquired during socrates. *Journal of Geophysical Research:
 Atmospheres*, 126. doi: <https://doi.org/10.1029/2020JD034482>
- Delanoë, J., Protat, A., Vinson, J., Brett, W., Caudoux, C., Bertrand, F., ...
 Dupont, J. (2016). BASTA: A 95-GHz FMCW Doppler Radar for Cloud
 and Fog Studies. *Journal of Atmospheric and Oceanic Technology*, 33. doi:
<https://doi.org/10.1175/JTECHD-15-0104.1>
- Diao, M. (2018). *Calibration of the vertical cavity surface emitting laser (vcSEL) wa-
 ter vapor hydrometer.* (<http://works.bepress.com/minghui-diao/50/>)
- Finlon, J. A., Rauber, R. M., Wu, W., Zaremba, T. J., McFarquhar, G. M., Nesbitt,
 S. W., ... DeMott, P. J. (2020). Structure of an Atmospheric River Over
 Australia and the Southern Ocean: II. Microphysical Evolution. *Journal of
 Geophysical Research Atmospheres*, 125. doi: 10.1029/2020JD032514
- Gottelman, A., Bardeen, C. G., McCluskey, C., Järvinen, E. J., Stith, J., Bretherton,
 C., ... Wu, W. (2020). Simulating Observations of Southern Ocean Clouds
 and Implications for Climate. *Journal of Geophysical Research: Atmospheres*,
 125. doi: 10.1029/2020JD032619
- Gottelman, A., Hannay, C., Bacmeister, J. T., Neale, R. B., Pendergrass, A. G.,
 Danabasoglu, G., ... Mills, M. J. (2019). High climate sensitivity in the com-
 munity earth system model version 2 (cesm2). *Geophysical Research Letters*,
 46. doi: <https://doi.org/10.1029/2019GL083978>
- Huang, Y., Chubb, T., Baumgardner, D., deHoog, M., Seims, S. T., & Manton,
 M. J. (2017). Evidence for secondary ice production in Southern Ocean open
 cellular convection. *Quarterly Journal of the Royal Meteorological Society*, 143.
 doi: 10.1002/qj.3041
- Huang, Y., Protat, A., Siems, S. T., & Manton, M. J. (2015). A-Train Observa-
 tions of Maritime Midlatitude Storm-Track Cloud Systems: Comparing the
 Southern Ocean against the North Atlantic. *Journal of Climate*, 28. doi:
[10.1175/JCLI-D-14-00169.1](https://doi.org/10.1175/JCLI-D-14-00169.1)
- Huang, Y., Siems, S. T., & Manton, M. J. (2021). Wintertime in situ cloud micro-
 physical properties of mixed-phase clouds over the southern ocean. *Journal
 of Geophysical Research: Atmospheres*, 126. doi: <https://doi.org/10.1029/2021JD034832>
- Huang, Y., Siems, S. T., Manton, M. J., Protat, A., Majewski, L., & Nguyen,
 H. (2019). Evaluating Himawari-8 Cloud Products Using Shipborne
 and CALIPSO Observations: Cloud-Top Height and Cloud-Top Tem-
 perature. *Journal of Atmospheric and Oceanic Technology*, 36. doi:
[10.1175/JTECH-D-18-0231.1](https://doi.org/10.1175/JTECH-D-18-0231.1)
- Järvinen, E., McCluskey, C., Waitz, F., Schnaiter, M., Bansemer, A., Bardeen, C.,
 ... DeMott, P. (2022, Under Review). Ice crystal properties and evidence
 for secondary ice production in southern ocean stratiform clouds. *Journal of
 Geophysical Research*.
- Kay, J. E., Wall, C., Yettella, V., Medeiros, B., Hannay, C., Caldwell, P., & Bitz,
 C. (2016). Global Climate Impacts of Fixing the Southern Ocean Shortwave
 Radiation Bias in the Community Earth System Model (CESM). *Journal of
 Climate*, 29. doi: 10.1175/JCLI-D-15-0358.1
- Kelleher, M. K., & Grise, K. M. (2019). Examining southern ocean cloud control-
 ling factors on daily time scales and their connections to midlatitude weather
 systems. *Journal of Climate*, 32. doi: 10.1175/JCLI-D-18-0840.1
- Kikuchi, K., Kameda, T., Higuchi, K., & Yamashita, A. (2013). A global classifica-

- 767 tion of snow crystals, ice crystals, and solid precipitation based on observations
 768 from middle latitudes to polar regions. *Atmospheric Research*, 132-133. doi:
 769 <https://doi.org/10.1016/j.atmosres.2013.06.006>
- 770 Klepp, C., Michel, S., Protat, A., Burdanowitz, J., Albern, N., Kähnert, M., ...
 771 Buehler, A. (2018). OceanRAIN, a new in-situ shipboard global ocean surface-
 772 reference dataset of all water cycle components. *Scientific Data*, 5. doi:
 773 <https://doi.org/10.1038/sdata.2018.122>
- 774 Lance, S., Brock, C. A., Rogers, D., & Gordon, J. A. (2010). Water droplet calibra-
 775 tion of the cloud droplet probe (cdp) and in-flight performance in liquid, ice
 776 and mixed-phase clouds during arcpac. *Atmospheric Measurement Techniques*,
 777 3. doi: 10.5194/amt-3-1683-2010
- 778 Lang, F., Ackermann, L., Huang, Y., Truong, S. C. H., Siems, S. T., & Manton,
 779 M. J. (2022). A climatology of open and closed mesoscale cellular convection
 780 over the southern ocean derived from himawari-8 observations. *Atmospheric*
 781 *Chemistry and Physics*, 22. Retrieved from [https://acp.copernicus.org/](https://acp.copernicus.org/articles/22/2135/2022/)
 782 [articles/22/2135/2022/](https://acp.copernicus.org/articles/22/2135/2022/)
- 783 Lang, F., Huang, Y., Protat, A., Truong, S. C. H., Siems, S. T., & Manton, M. J.
 784 (2021). Shallow convection and precipitation over the southern ocean: A
 785 case study during the capricorn 2016 field campaign. *Journal of Geophysical*
 786 *Research: Atmospheres*, 126. doi: <https://doi.org/10.1029/2020JD034088>
- 787 Lang, F., Huang, Y., Siems, S., & Manton, M. (2018). Characteristics of the ma-
 788 rine atmospheric boundary layer over the Southern Ocean in response to the
 789 synoptic forcing. *Journal of Geophysical Research: Atmospheres*, 123. doi:
 790 <https://doi.org/10.1029/2018JD028700>
- 791 Lang, F., Huang, Y., Siems, S. T., & Manton, M. J. (2020). Evidence of a Diurnal
 792 Cycle in Precipitation over the Southern Ocean as Observed at Macquarie
 793 Island. *Atmosphere*, 11. doi: 10.3390/atmos11020181
- 794 Mace, G. G., & Protat, A. (2018a). Clouds over the Southern Ocean as Observed
 795 from the R/V Investigator during CAPRICORN. Part I: Cloud Occurrence
 796 and Phase Partitioning. *Journal of applied meteorology and climatology*, 57.
 797 doi: 10.1175/JAMC-D-17-0194.1
- 798 Mace, G. G., & Protat, A. (2018b). Clouds over the Southern Ocean as Observed
 799 from the R/V Investigator during CAPRICORN. Part II: The Properties of
 800 Nonprecipitating Stratocumulus. *Journal of applied meteorology and climatol-*
 801 *ogy*, 57. doi: 10.1175/JAMC-D-17-0195.1
- 802 Mace, G. G., Protat, A., Humphries, R. S., Alexander, S. P., McRobert, I. M.,
 803 Ward, J., ... McFarquhar, G. M. (2021). Southern Ocean Cloud Properties
 804 Derived from CAPRICORN and MARCUS Data. *Journal of Geophysical*
 805 *Research: Atmospheres*, 125. doi: 10.1029/2020JD033368
- 806 Marchand, R., Wood, R., Bretherton, C., McFarquhar, G. M., Protat, A., Quinn, P.,
 807 ... Weller, B. (2014). The Southern Ocean Clouds, Radiation, Aerosol trans-
 808 port Experimental Study (SOCRATES). In *Workshop on clouds, aerosols,*
 809 *radiation and air-sea interface of the southern ocean. establishing directions for*
 810 *future research.*
- 811 Mason, S., Fletcher, J. K., Haynes, J. M., Franklin, C., Protat, A., & Jakob, C.
 812 (2015). A Hybrid Cloud Regime Methodology Used to Evaluate Southern
 813 Ocean Cloud and Shortwave Radiation Errors in ACCESS. *Journal of Cli-*
 814 *mate*, 28. doi: <https://doi.org/10.1175/JCLI-D-14-00846.1>
- 815 McCoy, I. L., Bretherton, C. S., Wood, R., Twohy, C. H., Gettelman, A., Bardeen,
 816 C. G., & Toohey, D. W. (2021). Influences of recent particle formation
 817 on southern ocean aerosol variability and low cloud properties. *Journal*
 818 *of Geophysical Research: Atmospheres*, 126. doi: [https://doi.org/10.1029/](https://doi.org/10.1029/2020JD033529)
 819 [2020JD033529](https://doi.org/10.1029/2020JD033529)
- 820 McFarquhar, G. M., Baumgardner, D., Bansemmer, A., Abel, S. J., Crosier, J.,
 821 French, J., ... Dong, J. (2017). Processing of ice cloud in situ data collected

- 822 by bulk water, scattering, and imaging probes: Fundamentals, uncertainties,
 823 and efforts toward consistency. *Meteorological Monographs*, 58, 11.1 - 11.33.
 824 doi: 10.1175/AMSMONOGRAPHS-D-16-0007.1
- 825 McFarquhar, G. M., Bretherton, C., Marchand, R., Protat, A., DeMott, P. J.,
 826 Alexander, S. P., . . . McDonald, A. (2021). Observations of Clouds, Aerosols,
 827 Precipitation, and Surface Radiation over the Southern Ocean: An Overview of
 828 CAPRICORN, MARCUS, MICRE, and SOCRATES. *Bulletin of the American*
 829 *Meteorological Society*, 102. doi: 10.1175/BAMS-D-20-0132.1
- 830 McFarquhar, G. M., Finlon, J. A., Stechman, D. M., Wu, W., Jackson, R. C., &
 831 Freer, M. (2018, jun). *University of Illinois/Oklahoma Optical Array Probe*
 832 *(OAP) Processing Software*. Zenodo. doi: 10.5281/zenodo.1285969
- 833 McFarquhar, G. M., Um, J., & Jackson, R. (2013). Small cloud particle shapes in
 834 mixed-phase clouds. *Journal of Applied Meteorology and Climatology*, 52. doi:
 835 10.1175/JAMC-D-12-0114.1
- 836 Murray, R. J., & Simmonds, I. (1991). A numerical scheme for tracking cyclone centres
 837 from digital data. part i: development and operation of the scheme. *Australian*
 838 *Meteorological Magazine*, 39.
- 839 Müllenstädt, J., Salzmann, M., Kay, J., Zelinka, M., Ma, P., Nam, C., . . . Quaas,
 840 J. (2021). An underestimated negative cloud feedback from cloud life-
 841 time changes. *Nature Climate Change*, 11. doi: [https://doi.org/10.1038/
 842 s41558-021-01038-1](https://doi.org/10.1038/s41558-021-01038-1)
- 843 Naud, C. M., Booth, J. F., & Del Genio, A. D. (2014). Evaluation of ERA-interim
 844 and MERRA cloudiness in the Southern Ocean. *Journal of Climate*, 27. doi:
 845 10.1175/JCLI-D-13-00432.1
- 846 NCAR/EOL. (2023). Ncar hcr radar and hsrl lidar moments data. version 3.0.
 847 *UCAR/NCAR - Earth Observing Laboratory*. (Accessed: 2022-03-17) doi:
 848 <https://doi.org/10.5065/D64J0CZS>
- 849 Pepler, A. S., Dowdy, A. J., van Rensch, P., Rudeva, I., Catto, J. L., & Hope,
 850 P. (2020). The contributions of fronts, lows and thunderstorms to south-
 851 ern Australian rainfall. *Climate Dynamics*. doi: [https://doi.org/10.1007/
 852 s00382-020-05338-8](https://doi.org/10.1007/s00382-020-05338-8)
- 853 Protat, A., Schulz, E., Rikus, L., Sun, Z., Xiao, Y., & Keywood, M. (2017). Ship-
 854 borne observations of the radiative effect of Southern Ocean clouds. *Journal of*
 855 *Geophysical Research: Atmospheres*, 122. doi: 10.1002/2016JD026061
- 856 Schima, J., McFarquhar, G., Romatschke, U., Vivekanandan, J., D'Alessandro, J.,
 857 Haggerty, J., . . . Schaefer, E. (2022, In Preparation). Characterization of
 858 southern ocean boundary layer clouds using airborne radar, lidar, and in-situ
 859 cloud data: Results from socrates. *Journal of Geophysical Research*.
- 860 Schnaiter, M. (2018). Phips-halo stereo imaging data. version 1.0. *UCAR/NCAR*
 861 *- Earth Observing Laboratory*. (Accessed: 2020-10-01) doi: [https://doi.org/10.
 862 .5065/D62B8WWF](https://doi.org/10.5065/D62B8WWF)
- 863 Schnaiter, M., Järvinen, E., Abdelmonem, A., & Leisner, T. (2018). Phips-halo:
 864 the airborne particle habit imaging and polar scattering probe. part 2: Char-
 865 acterization and first results. *Atmospheric Measurement Techniques*, 11. doi:
 866 10.5194/amt-11-341-2018
- 867 Thompson, G., Field, P. R., Rasmussen, R. M., & Hall, W. D. (2008). Explicit fore-
 868 casts of winter precipitation using an improved bulk microphysics scheme. part
 869 ii: Implementation of a new snow parameterization. *Monthly Weather Review*,
 870 136. doi: 10.1175/2008MWR2387.1
- 871 Truong, S., Huang, Y., Land, F., Messmer, M., Simmonds, I., Siems, S., & Manton,
 872 M. (2020). A climatology of the marine atmospheric boundary layer over the
 873 Southern Ocean from four field campaigns during 2016 – 2018. *Journal of*
 874 *Geophysical Research Atmospheres*, 125. doi: 10.1029/2020JD033214
- 875 UCAR/NCAR - EOL. (2014). *Hiaper cloud radar (hcr)* (Tech. Rep.). doi: [https://
 876 doi.org/10.5065/D6BP00TP](https://doi.org/10.5065/D6BP00TP)

- 877 UCAR/NCAR EOL. (2018). *Capricorn r/v investigator 95-ghz doppler cloud radar*
 878 *(basta) level 2 data*. (Accessed: 2020-12-01) doi: [https://data.eol.ucar.edu/](https://data.eol.ucar.edu/dataset/552.038)
 879 [dataset/552.038](https://data.eol.ucar.edu/dataset/552.038)
- 880 UCAR/NCAR EOL. (2019). *Socrates: Low rate (lrt - 1 sps) navigation, state pa-*
 881 *rameter, and microphysics flight-level data. version 1.3*. (Accessed: 2020-10-01)
 882 doi: <https://doi.org/10.5065/D6M32TM9>
- 883 Vivekanandan, J., Ellis, S., Tsai, P., Loew, E., Lee, W.-C., Emmett, J., ... Rauen-
 884 buehler, S. (2015). A wing pod-based millimeter wavelength airborne cloud
 885 radar. *Geoscientific Instrumentation, Methods and Data Systems*, 4. doi:
 886 [10.5194/gi-4-161-2015](https://doi.org/10.5194/gi-4-161-2015)
- 887 Wang, Y., McFarquhar, G. M., Rauber, R. M., Zhao, G., Wu, W., Finlon, J. A., ...
 888 Toohey, D. W. (2020). Microphysical Properties of Generating Cells Over the
 889 Southern Ocean: Results From SOCRATES. *Journal of Geophysical Research*
 890 *Atmospheres*, 125. doi: [10.1029/2019JD032237](https://doi.org/10.1029/2019JD032237)
- 891 Wang, Z., Siems, S. T., Belusic, D., Manton, M. J., & Huang, Y. (2015). A cli-
 892 matology of the precipitation over the southern ocean as observed at mac-
 893 quarie island. *Journal of Applied Meteorology and Climatology*, 54. doi:
 894 [10.1175/JAMC-D-14-0211](https://doi.org/10.1175/JAMC-D-14-0211).
- 895 Williams, K., Bodas-Salcedo, A., Déqué, M., Fermepin, S., Medeiros, B., Jakob,
 896 C., ... Williamson, D. L. (2013). The Transpose-AMIP II Experiment
 897 and Its Application to the Understanding of Southern Ocean Cloud Biases
 898 in Climate Models. *Journal of Climate*, 26. doi: [https://doi.org/10.1175/](https://doi.org/10.1175/JCLI-D-12-00429.1)
 899 [JCLI-D-12-00429.1](https://doi.org/10.1175/JCLI-D-12-00429.1)
- 900 Wu, W., & McFarquhar, G. M. (2016). On the impacts of different definitions
 901 of maximum dimension for nonspherical particles recorded by 2d imag-
 902 ing probes. *Journal of Atmospheric and Oceanic Technology*, 33. doi:
 903 <https://doi.org/10.1175/JTECH-D-15-0177.1>
- 904 Wu, W., & McFarquhar, G. M. (2019). Sf/ncar gv hiaper fast 2dc particle size
 905 distribution (psd) product data. version 1.1. *UCAR/NCAR - Earth Observing*
 906 *Laboratory*. (Accessed: 2020-10-01) doi: [https://doi.org/10.26023/E95A-FKYF-](https://doi.org/10.26023/E95A-FKYF-7P0R)
 907 [-7P0R](https://doi.org/10.26023/E95A-FKYF-7P0R)
- 908 Yuter, S. E., & Houze, R. A. J. (1995). Three-dimensional kinematic and mi-
 909 crophysical evolution of florida cumulonimbus. part ii: Frequency distribu-
 910 tions of vertical velocity, reflectivity, and differential reflectivity. *Monthly*
 911 *Weather Review*, 123. doi: [https://doi.org/10.1175/1520-0493\(1995\)123<1941:](https://doi.org/10.1175/1520-0493(1995)123<1941:TDKAME>2.0.CO;2)
 912 [TDKAME>2.0.CO;2](https://doi.org/10.1175/1520-0493(1995)123<1941:TDKAME>2.0.CO;2)
- 913 Zaremba, T. J., Rauber, R. M., McFarquhar, G. M., Hayman, M., Finlon, J. A.,
 914 & Stechman, D. M. (2020). Phase Characterization of Cold Sector South-
 915 ern Ocean Cloud Tops: Results from SOCRATES. *Journal of Geophysical*
 916 *Research: Atmospheres*, 125. doi: [10.1029/2020JD033673](https://doi.org/10.1029/2020JD033673)
- 917 Zelinka, M. D., Myers, T. A., McCoy, D. T., Po-Chedley, S., Caldwell, P. M., Ceppi,
 918 P., ... Taylor, K. E. (2020). Causes of higher climate sensitivity in cmip6
 919 models. *Geophysical Research Letters*, 47. doi: [https://doi.org/10.1029/](https://doi.org/10.1029/2019GL085782)
 920 [2019GL085782](https://doi.org/10.1029/2019GL085782)
- 921 Zhou, X., R., A., L., M. I., Bretherton, C. S., Bardeen, C., Gettelman, A., ... Ming,
 922 Y. (2020). Evaluation of cloud and precipitation simulations in CAM6 and
 923 AM4 using observations over the Southern Ocean. *Earth and Space. Earth and*
 924 *Space Science*. doi: <https://doi.org/10.1029/2020EA001241>